Study of the Response of a New Continuous Compressionless Bubble Chamber

by

Noel Alberto Cruz Venegas

A thesis submitted in partial fulfillment of the requirements for the degree of

Master of Science

Department of Physics

University of Alberta

Abstract

Bubble chambers filled with fluorocarbons are a world-leading technology to search for nuclear recoils produced by spin-dependent WIMP dark matter particles. In this work, a novel bubble chamber using 28 ± 1 ml of the fluorocarbon C_5F_{12} as target material is investigated. This superheated liquid detector nucleates bubbles as the result of elastic scattering off nuclei with neutral particles for example dark matter or neutrons.

As the chamber produces small eruptions at the top, when a nuclear recoil happens inside the superheated liquid, it was named Geyser, like the geothermal phenomenon. The C_5F_{12} Geyser bubble chamber does not require to be pressurized after every event to restore the active liquid. Instead, it uses a combination of gravity and temperature gradient to achieve an almost continuously superheated state.

The whole apparatus, also referred to as a compressionless bubble chamber, was exposed to neutrons coming from an AmBe source. In a live-time of 2.45 ± 0.03 hours, the detector demonstrated evidence of AmBe neutron recoil events. A comparison of a Geant4 Monte Carlo simulation of the same detector, allowed for the calculation of dead time ($\tau = 27.9 \pm 3.0$ seconds) and detector efficiency (ϵ) of 56.5 ± 5.0 %.

Preface

The C_5F_{12} Geyser or compressionless bubble chamber apparatus was constructed by Pitam Mitra and operated by several summer students at the University of Alberta in 2014, 2016 and 2018.

My main contribution to the C_5F_{12} Geyser experiment regarding the work of this thesis consisted of performing the data analysis of the neutron calibration and background runs for this apparatus. I also built and coded entirely the C_5F_{12} Geyser Geant4 Monte Carlo simulation.

The following software and packages were used for data processing and figure creation: Python (*with Numpy, Scipy, Matplotlib, Glob, Pandas, Statistics, Root Pandas*).

The extraction of thermodynamical parameters was done using PICOcode. This software was developed by members of the PICO Collaboration that uses bubble chambers for WIMP dark matter searches.

I built and designed the algorithm for event definition as a result of pressure increases in the superheated C_5F_{12}. I ensured data quality and helped to improve and update the C_5F_{12} Geyser DAQ software (Arduino code).

I also worked alongside with Dr. Sumantal Pal in the construction of the hydraulic system. David Biaré participated and fully developed the LabVIEW VI program to operate this system. Ben Broerman from Queen's University provided the bellows transfer accumulator that was connected between the hydraulic system and the C_5F_{12} Geyser.

I certify that this thesis was composed by myself, that the work contained here is my own except where explicitly stated otherwise in the text.

I declare that this work has not been submitted for any other degree or professional qualification except as specified.

Dedicated to my friend Jose Parra who passed away,
neutrinos are getting closer ...

Acknowledgements

In the first place, I would like to acknowledge my main supervisor Carsten Krauss and co-supervisor Marie Cécile Piro. For their time, tremendous patience, trust and effort invested through the definition and evolution of my MSc thesis work.

I am immensely indebted to Carsten Krauss for helping to figure out how to bridge the gap of where I was and where I needed to be. This was a particularly difficult task due to the various complications caused by the 2020 pandemic.

I received a lot of help and resources from Scott Fallows, to whom I acknowledge his patience and guidance provided while understanding the C_5F_{12} Geyser setup.

I also need to acknowledge Sumanta Pal, for taking the lead in the construction of the hydraulic system and show me through example how to do things in the lab environment.

While building the software for the hydraulic system, I would like to show my appreciation and acknowledgement to David Biaré. He came to build from scratch and complete the Lab-VIEW interface I was working on as well as to rebuild the electrical diagram. In the end, he was the main actor behind making this running.

Special mention goes to Jason Dibbs of the glass blowing shop. His expertise in glassblowing played an irreplaceable role in the fabrication and repair of the C_5F_{12} Geyser.

I would like to thank the University of Alberta's Department of Physics and the PICO Collaboration for offering me a significant amount of opportunities to grow up a scientist in preparation.

I acknowledge the Mitacs Globalink Graduate Fellowship for providing me with scholarship funding, and thank them for being the conduit for the various learning, enriching and personal development experiences in Canada.

Finally but not less important, to my parents, family and friends. For being there and show me your support and love through the up and downs in Edmonton. To you, my Sister Yuli, and Mario, my little brother!

Contents

List of Tables

List of Figures

Chapter 1

Introduction

1.1 Dark Matter

For the last century many cosmological observations, have concluded that more than 80 % of the matter in the Universe is non-luminous or dark.

The only observable effect of its existence is its gravitational influence on stars, galaxies, large-scale structures of the Universe, and the Cosmic Microwave Background (CMB). Based on these observations, the so-called $\lambda - CDM$ (Lambda cold dark matter model) establishes the following: Our Universe is flat [1] and is composed of (4.56 $\pm$ 0.16) % baryonic matter, (22.7 $\pm$ 1.4) % dark matter and (72.8 $^{+1.5}_{-1.6}$) % dark energy [1].

The properties of dark matter are well understood in the Cosmological $\lambda - CDM$ model but there are no particles with those properties in the Standard Model of Particle Physics. What could dark matter be made of?

Discovering the nature of dark matter is synonymous with getting access to physics beyond the Standard Model of Particle Physics. It has become one of the greatest scientific puzzles to solve in the XXI century.

1.2 Astrophysical evidence of dark matter

In astrophysics, there is plenty of evidence that supports the existence of dark matter. For instance, the dark matter density calculated from the cosmic microwave background requires it to be stable to explain the flatness of the

[1] In that geometry of space, a drawn triangle's angles add up to 180^o and the Pythagorean theorem holds.

current Universe [1], and the abundance of light elements in the early Universe requires dark matter to be non baryonic [2]. Additional pieces of astrophysical evidence and how constraints to dark matter properties are presented in the following sections.

1.2.1 Rotation curves

One of the most convincing probes of dark matter comes from rotation curves spiral galaxies. The visible part of spiral galaxies consists of a spherical protuberance in the centre and a thin elongated disc at their extremes [3]. The tangential velocity v_r of a star with a mass m that orbits a galaxy with mass M_r to a distance r from the galactic centre is obtained by matching the gravitational and centripetal forces.

$$\frac{mv_r^2}{r} = \frac{GmM_r}{r^2} \tag{1.1}$$

leading to a tangential velocity around the galactic center:

$$v_r = \sqrt{\frac{GM_r}{r}} \tag{1.2}$$

Equation 1.2, predicts that stars move slower the further they are away from the center of their galaxy. The first test of this model was made by Fritz Zwicky in 1930 [4]. He used the Virial theorem to estimate the mass of the Coma galaxy cluster. He found that the mass was 400 times more than the mass obtained from the luminosity of the galaxies contained in the cluster. Fritz Zwicky named the invisible matter dark matter.

40 years later, in the 1970s, the American Astronomer Vera Rubin measured v_r in the Milky Way and other galaxies, she measured the speed of stars at the periphery of the galaxy by Doppler shift (21 cm Hydrogen line) and she estimated its mass. This mass was compared to the visible mass. She found that additional mass must be providing a gravitational pull to account for the dynamics of the cluster (see figure 1.1).

The observations made, suggest that the rotation speeds are constant until large radii from the centre of the galaxies instead of decreasing according to

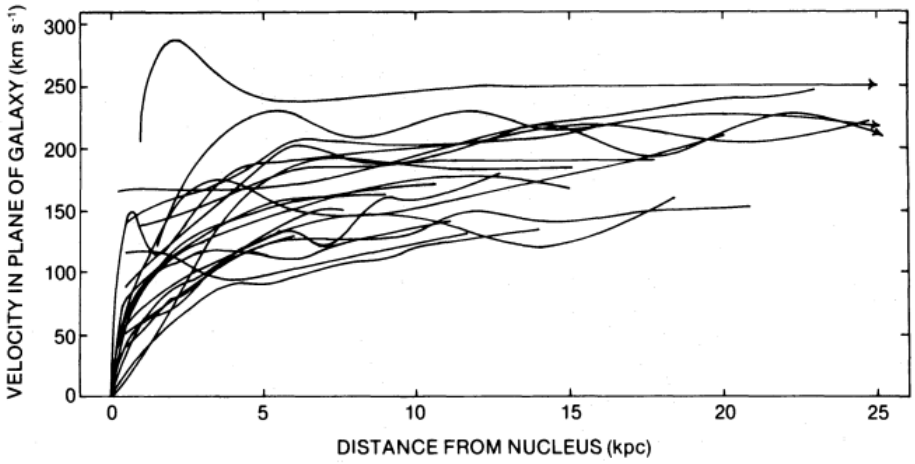

Figure 1.1: Rotation curves of spiral galaxies as measured by Vera Rubin [3]. Most of the galaxies show a flattening at a large distance from the center.

equation 1.2. The only way to explain these discrepancies is that the visible part of the galaxy is immersed in a spherical Dark Matter halo (DM halo) that contributes to 80-90% of the total mass [5].

1.2.2 Weak field lensing of colliding galaxy clusters

Based on the studies of stellar object dynamics through gravitational lensing [5], it has been concluded that dark matter interacts with normal matter through gravity.

On the other hand, galaxy dynamic collisions allow inferring that dark matter cannot be explained by modifications to gravity [6]. The most compelling evidence of this comes from the Bullet Cluster [7] and MACS J0025.4-1222 [8]. The aforementioned clusters, were created each one by the collision in the past of two galaxy clusters.

Studies with gravitational lensing and X-ray images revealed that the majority of the hydrogen is within the region near the centre of the clusters while most of the mass is distributed near the edges. This phenomenon can not be explained by theories that modify the general theory of relativity.

1.2.3 Cosmic large structure of the Universe

The cosmic large structure of the Universe from simulations of the structures formation, is in agreement with the astronomical observations if the dark matter is not relativistic.

To survey the distribution of dark matter, the experiments 2DFGRS (2-degree Field Redshift Survey) and SDSS (Sloan Digital Sky Survey) mapped the spatial distribution of galaxy clusters and the physical properties of galaxies with low redshift [9].

Both experiments concluded that the distribution of distant galaxies is not scattered randomly. But instead, there is a network of filaments surrounding wide regions of empty space. This structure, cannot be explained by the gravitational clumping of ordinary matter [10]. Under the hypothesis of the abundance of dark matter weakly interacting particles before baryogenesis, it can be asserted that their coupling occurred before thermal equilibrium [5].

Computational simulations strongly suggest that dark matter is needed for explaining the cosmic large structure of the Universe. The Virgo Consortium, for Cosmological Supercomputer Simulations, performed an N-body simulation with $N = 2160^3 \times 10^{10}$. Each particle simulated represented a dark matter of approximately a billion solar masses.

The results obtained imitate the cosmic structure observed by 2DFGRS and SDSS if the dark matter in the model is considered non-relativistic or cold [11].

1.3 Beyond the Standard Model

Dark matter is an unknown type of matter composed of particles beyond the Standard Model of particle physics. Candidate particles for dark matter naturally arise in a lot of theories beyond the Standard Model of particle physics and from strong astrophysical constraints. Figure 1.2 summarizes the candidates over a large range of masses.

A generic weakly interacting massive particle (WIMP) is one of the most attractive candidates to account for the cold dark matter in our Universe since

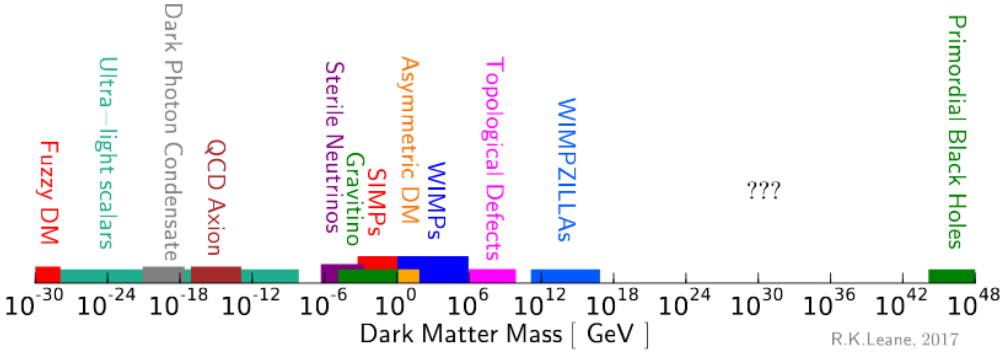

Figure 1.2: Candidates for dark matter particles can be found in a range from 10^{-31} GeV until 10^{48} GeV [18].

it would be thermally produced with the correct abundance to account for the observed dark matter density [12].

Axions are also preferred dark matter candidates since they solve the strong CP problem in the Standard Model [13]. Together with the ALP (Axions Like Particle) and dark photons, they receive the name WISP (Weakly Interacting Sub-eV Particles) [14]. Experiments, such as PVLAS [15], CAST [16] and ADMX [17] use resonating cavities of adjustable resonance frequency to search for WISPs.

1.4 WIMP

The WIMP is a well motivated candidate for dark matter [19]. It is a particle that interacts weakly, and its expected mass range is from GeV to TeV. These particles are assumed to be in thermal equilibrium with quarks and leptons in the hot early universe and decoupled when they were non-relativistic. As a result, they annihilate giving rise to a relic density that is consistent with the observed dark matter density [19].

Theoretical particle physics models contain particles that naturally satisfy the requirements for a WIMP. Specifically, in supersymmetric models (SUSY) the lightest supersymmetric particle in theories with R-parity conservation is a good dark matter candidate. However, supersymmetric particles have not

yet been observed.

1.4.1 WIMP elastic scattering off nuclei

If the Milky Way's DM halo is composed of WIMPs, then the WIMP flux on the Earth is of the order of $10^5\ cm^{-2}s^{-1}$ for a WIMP mass of 100 GeV [20]. This flux could be detected via nuclear recoils in Earth-based detectors, caused by WIMP elastic scattering. More specifically, direct dark matter search experiments aim to measure the rate R, and energy of the nuclear recoils E_R. For incoming WIMPs of number density n (astrophysical WIMP distribution) and uniform velocity v, the scatter rate off a single nuclei target can be described as:

$$R = \sigma n v \tag{1.3}$$

where σ is the interaction cross-section for a particular target material. Lewin and Smith [21], outlined a standard procedure for which the expected WIMP recoil spectrum can be calculated. They provided calculations for coherent scattering and assume σ has spin-dependent and spin-independent components.

The spin-independent cross-section is given by:

$$\sigma^{SI} = \frac{4}{\pi}\mu_A^2 \left(Z f_p + (A - Z) f_n\right)^2 \tag{1.4}$$

where Z is the number of protons, μ_A is the WIMP-nucleus reduced mass, and f_p and f_n are the coupling of the proton and neutron respectively [22].

The cross-section for experiments searching for spin-dependent coupling to dark matter, is given by:

$$\sigma^{SD} = \frac{32}{\pi} G_F^2 \mu_A^2 \left[a_p \langle S_p \rangle + a_n \langle S_n \rangle\right]^2 \frac{J(J+1)}{J^2} \tag{1.5}$$

where a_p and a_n are the proton and neutron coupling strengths and, $\langle S_p \rangle$ & $\langle S_n \rangle$ the spin expectation values for proton and neutron spin in the target nucleus. Finally, J is the total nuclear spin.

Nucleus	Z	Odd Nucleon	J	$\langle S_p \rangle$	$\langle S_n \rangle$
^{19}F	9	p	1/2	0.477	-0.004
^{23}Na	11	p	3/2	0.248	0.020
^{27}Al	13	p	5/2	-0.343	0.030
^{29}Si	14	n	1/2	-0.002	0.130
^{35}Cl	17	p	3/2	-0.083	0.004
^{39}K	19	p	3/2	-0.180	0.050
^{73}Ge	32	n	9/2	0.030	0.378
^{93}Nb	41	p	9/2	0.460	0.080
^{125}Te	52	n	1/2	0.001	0.287
^{127}I	53	p	5/2	0.309	0.075
^{129}Xe	54	n	1/2	0.028	0.359
^{131}Xe	54	n	3/2	-0.009	-0.227

Table 1.1: Table of proton and neutron spin expectation values of selected stable isotopes with non-zero spin. Notice the large value of $\langle S_p \rangle$ for targets with fluorine (^{19}F) [18].

The WIMP nuclear recoil spectrum depends on the target material and the mass of the WIMP candidate. Therefore, the WIMP nuclear recoil depends on the energy deposition in the target nuclei used (see table 1.1). Additionally, the WIMP event rate is modulated as a result of the Earth's motion and position through the Milky Way's DM halo [23].

The WIMP could also be detected indirectly by observing the annihilation products at locations where the WIMPs should be abundant (centre of the Sun, the Milky Way's core and dwarf galaxies). The experiments will look for a surplus of standard model particles such as neutrinos, gammas rays, etc [24].

Another channel of detection is via the production of WIMPs in accelerators. If the center of mass-energy at proton-proton collisions surpasses the mass of a WIMP, dark matter particles could be produced, allowing the study of their fundamental properties (mass, cross-section, spin, decay modes, etc)[25]. Even if this detection is possible, the unknown dark matter mass makes it challenging to infer the kinematic distributions of such an interaction.

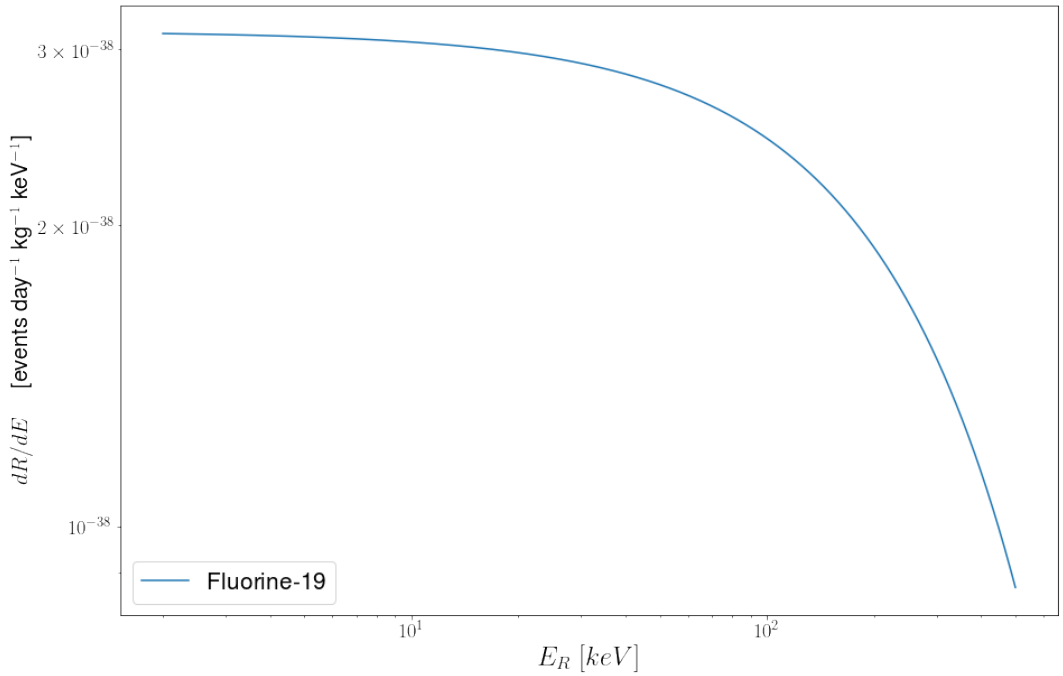

Figure 1.3: The differential event rate in fluorine target for a 100 GeV WIMP with $\sigma = 3 \times 10^{-46}\ cm^2$ using standard astrophysical assumptions [21].

1.4.2 Direct WIMP detection

Goodman and Witten were the first to propose that a WIMP can be detected by elastic scattering off nuclei in a terrestrial detector [26].

Earth-based direct detection experiments benefit from the movement of the solar system around the galactic center through the DM halo. As a result, a flux of WIMPs travels through the terrestrial detector (local density = 0.3 GeV/cm^3 [27]), scattering off an atomic nucleus with an average velocity of 300 km/sec [20].

However, the differential event rate R is difficult to measure as shown in figure 1.3. The WIMPs scattering off nuclei is investigated using four separated (or combined) channels of detection: charge, scintillation light, and heat. The heat can manifest as phonons in cryogenic crystals and as bubbles in superheated liquids (for a detailed review, see [28]). A brief description of those technologies is as follows:

- **Noble gas detectors (charge and scintillation signals):**
  Consist of liquid noble gases that scintillate. The noble liquid glows in the ultraviolet wavelength spectrum allowing for efficient detection by photomultiplier tubes at the walls of the experiment. PANDA-X [29], LZ [30], LUX [31], XENON1T [32], DEAP3600 [33] and DarkSide [34] are examples of experiments using this technology.

  Xenon based detectors use double-phase (liquid and gas) TPC (Time Projection Chamber) to discriminate electron recoils (LZ [30], XENON1T [32], XENONnT [35] and DARWIN [36]) against nuclear recoils. Argon-based experiments use pulse shape discrimination for the same purpose (DEAP3600 [33] and the double phase argon TPC DarkSide [37]).

- **Scintillating crystals**
  Consist of materials that exhibit scintillation light when excited by ionizing radiation. For instance, the DAMA/LIBRA [38] experiment uses NaI crystals. It has reported an annual modulation consistent with a WIMP explanation since 1995. However, that signal has been excluded

by many other WIMP experiments and is still unexplained.

Scintillation in crystals due to nuclear recoils can be statistically separated from events caused by electron recoil events using pulse shape discrimination.

- **Cryogenic solid-state detectors**

  Are detectors at which the active material is maintained at millikelvin temperatures (< 20 mK). This allows the detection of phonons from the interaction of a single particle in a crystal lattice.

  These detectors discriminate electron recoils from nuclear recoils on an event-by-event basis by complementary channels (scintillation, phonon, ionization, etc). Leading experiments of this class are CDMS [39] with Ge and Si, EDELWEISS with Ge and CRESST [40] with calcium tungstate (WO_4Ca).

- **Superheated liquid detectors:**

  This kind of detector uses moderately superheated liquid as active mass. A local energy deposition will induce bubble nucleation. The main advantage is that under specific conditions of temperature and pressure these detectors are insensitive to electromagnetic backgrounds [41]. Additional virtues include easy replacement of target liquid as well as sensitivity to spin-dependent nucleon-WIMP interactions when used with fluorine enriched target materials.

  Event discrimination between alpha recoils and nuclear recoils is done by acoustic discrimination of the bubble formation. In parallel, nuclear recoil events are distinguished visually from events due to neutrons which often cause multiple scattering. Some examples are the superheated droplet detectors (SIMPLE [42] and PICASSO [43]) and the PICO bubble chambers with C_3F_8 and CF_3I targets [44]–[46].

The experimental challenge in WIMP dark matter detectors is to detect keV nuclear recoil energies due to elastic scattering with atom nuclei. On this

scale, there are subatomic phenomena that mimic the nuclear recoil WIMP signal and are more probable.

Background mitigation involves the elimination of any source of particles that could produce a similar signal (mainly due to natural radioactivity). Locating the WIMP dark matter search experiments underground provides a first protection level since cosmic rays get absorbed in rock [47]. Immersing the detector in ultra-pure water reduces gamma rays and neutrons from surrounding material. Additional background protection comes from a selection of radiopure materials.

The PICO bubble chambers (superheated liquid detectors) have established world-leading limits for WIMP-proton spin-dependent interactions [44][45][46]. Additionally, these detectors provide excellent discrimination against electromagnetic backgrounds. To maximize the interaction rate from a potential WIMP nuclear recoil, the PICO Collaboration is constructing the PICO-500 bubble chamber. The next chapter introduces the fundamentals of this technology and how the compressionless bubble chamber of this work can help to improve the sensitivity to WIMP dark matter for chambers beyond PICO-500.

Chapter 2

Superheated liquid detection for WIMP and radiation interactions

2.1 Superheated liquid radiation detection

The use of visual techniques for exploring and studying elementary particles and their interactions has been key for the advance of nuclear and subnuclear physics. Before the invention of bubble chambers or superheated liquid detectors, cloud chambers and photographic nuclear emulsions were the first of these kinds of detectors.

In 1951, Donald Glaser invented the bubble chamber [1][48]. The principle of bubble chamber operation is based on a pressure-controlled fluid and above its boiling point or below its vapor pressure (superheated state).

When the energy deposited by a particle entering the superheated liquid breaks the metastable state, a localized macroscopic disturbance triggers a partial release of stored energy, i.e., it produce bubbles.

The bubble nucleated is recorded by the detector using cameras or acoustical sensor and then the bubble chamber is pressurized for a few seconds. Then, the detector is slowly expanded before reaching the working pressure and can detect another event. Due to this limitation on dead time, bubble chambers were supplanted in the mid-80s by wire chambers, spark chambers, drift chambers, and silicon detectors. Notwithstanding, bubble chambers in the second

[1] Physics Nobel Prize 1960.

half of the last century, successfully enabled the detection of new particles and discoveries within the Standard Model (evidence of the weak neutral current, and the discovery of many meson and baryon resonances) [49].

2.2 Detection of the WIMPs

Superheated liquid detectors are advantageous for WIMP dark matter searches due to their low sensitivity to minimally ionizing particles. This provides low electromagnetic backgrounds compared to detectors based on charge, scintillation light and phonon direct detection WIMP channels. For instance PICO bubble chambers for WIMP detection have demonstrated suppression of electron recoil events of about 10^{10} [41]. Additionally, superheated liquid detectors have the advantage of being safe to operate, low-cost, having an optimal target constitution, and allowing room-temperature operation (no cryogenics).

The idea of using moderately superheated liquids for detecting WIMP nuclear recoils dates back to the 1990s [50][51]. At that time, a bubble chamber as proof-of-principle was built at the University of Chicago [52]. This detector consisted of using 12 mL CF_3Br as a superheated liquid. The pressure in the chamber was controlled by a piston operated by compressed air. To avoid surface nucleation events, the superheated liquid was contained in a small quartz pressure vessel. To reconstruct the 3D bubble position, CCD cameras were used. This bubble chamber and features set the basis of the COUPP [53] (Chicagoland Observatory for Underground Particle Physics) and PICO projects.

Another type of superheated liquid detector is by using superheated droplet detectors. They were first explored as WIMP detectors by the SIMPLE [42] and PICASSO [43] collaborations. The PICASSO (Project in Canada to Search for Supersymmetric Objects), consisted of superheated micro-droplets of C_4F_{10} dispersed in a polymerized medium. This project pioneered the idea of using piezoelectric transducers to record the bubble sound signal. They discovered acoustic discrimination between alpha events and nuclear recoils [54].

2.2.1 PICO bubble chambers

The PICASSO and COUPP superheated liquid experiments merged into the PICO project in 2012. PICO is an international collaboration from institutions in Canada, the USA, Mexico, India, and the Czech Republic. The PICO bubble chambers are operated at the underground laboratory SNOLAB (6800 m.w.e.[2]) in Greater Sudbury, Ontario, Canada.

The first PICO detector was PICO-2L filled with C_3F_8 and was initially limited by particulate background [44]. A second PICO-2L fill was operated until 2016 showing that the background can be removed. To increase the sensitivity, a PICO detector with 37 kg of C_3FI was operated until 2014 [45]. In 2016, PICO-60 exchanged the active fluid with C_3F_8. PICO-60 published the world's best limits to WIMP-proton in spin-dependent interactions [46].

Since the disassembly of PICO-60 in 2017, most of the PICO collaboration effort has been focused on new chamber designs to eliminate the need for a water buffer directly in contact with the active fluid. By removing the water buffer, anomalous bubble nucleations due to the interface effects (chemical reactions and particle contamination) with the superheated liquid can be suppressed.

2.2.2 PICO buffer-free bubble chambers

PICO-40L is a PICO bubble chamber that follows PICO-60. Currently, undergoing commissioning, it benefits from enhanced background control. The jar that contains the superheated liquid is mounted in an inverted position ("right-side-up" design). This principle has been demonstrated by the Drexel PICO group and others [55].

In parallel, the PICO-500 bubble chamber is being designed and built for deployment at SNOLAB in 2022 and 2023. It will follow the same design as PICO-40L. The physics that can be achieved with this detector include sensitivity to coherent solar neutrino-nucleus scattering and potentially galactic

[2]Is the abbreviation of meter water equivalent. Is a standard measure of cosmic ray attenuation in underground laboratories. A laboratory at a depth of 1000 m.w.e. is shielded from cosmic rays similar to a lab 1000 m below the surface of a body of water.

supernova neutrinos [56].

PICO has also deployed several bubble chambers above ground for calibration purposes. All of them are designed with a small active volume as well as simple operation.

A case for the R&D free-buffer PICO bubble chambers is the Geyser bubble chamber. This type of bubble chamber operates at atmospheric pressure. The superheated state is obtained thermally (heat transfer) instead of mechanically by the action of a piston. Several Geyser prototypes were constructed and tested at the University of Montreal [57].

In 2010 the University of Alberta (UofA) group tested a Geyser based bubble chamber using alcohol [58]. The work of the current thesis is related a similar Geyser at UofA filled with C_5F_{12} instead. It was operated between 2016 and 2020 (see Chapters 3 and 4 for further details).

A group independent from PICO constructed a prototype Geyser at Milano-Bicocca with a mass of 0.5 kg C_3F_8 in 2013 (MOSCAB Collaboration [59]).

2.3 Bubble growth due to nuclear recoils in superheated liquid detectors

2.3.1 The Seitz Model

Glaser tried to explain bubble formation using electrostatic theory, but he did not succeed [48].

In 1958, Frederick Seitz explained this thermodynamic phenomenon with the Hot Spike Model [60]. This model postulates the energy entering the superheated liquid is converted into heat or "hot spike". Then the vapor pressure rises locally. This promotes the formation of a spherical cavity with radius R, aimed to minimize the surface tension between liquid/gas. The cavity volume to create a nucleation of radius R should be such that:

$$R < R_c = \frac{2\sigma}{p_v - p_l} \frac{\rho_l}{\rho_l - \rho_v} \tag{2.1}$$

where R_c is the critical radius, σ is the surface tension, p is the pressure, ρ the density and the indices v and l correspond to the vapor and liquid

property of the fluid respectively. The bubbles of radius $R < R_c$ will expand and grow to macroscopic size, while bubbles with $R > R_c$ will collapse due to surface tension. While equation 2.1 describes the general conditions for bubble formation, the nucleation mechanism depends on the type of particle interacting that recoils in the atomic nuclei or electron. The minimum energy needed E to form a bubble greater than or equal to R_c and equilibrium vapor pressure is given by:

$$E > E_c = \underbrace{4\pi R_c^2(\sigma - T\frac{\partial\sigma}{\partial T})}_{\text{surface term}} + \underbrace{\frac{4\pi}{3}R_c^3\rho_b(h_v - h_l)}_{\text{volume term}} - \underbrace{\frac{4\pi}{3}R_c^3(p_v - p_l)}_{\text{reversible work}} \tag{2.2}$$

where E_c is the critical energy, T is the temperature, and h is the specific enthalpy. In equation 2.2, the surface term represents the energy required to balance the surface tension. The latent heat needed to boil a sphere of fluid within the critical radius R_c is described as the volume term. Finally, the reversible work done in expanding the bubble is the last term. If the energy deposited is enough ($E > E_c$), the bubble will be able to expand and vaporize the liquid. Otherwise, the bubble will collapse and the phase transition will not occur.

Therefore, to generate a complete phase transition, the Seitz Model established that the energy supplied E_{dep} to the superheated liquid must be deposited inside the critical radius R_c and larger than critical energy E_c such that $E_{dep} > E_c$.

In a superheated liquid detector, E_c can be chosen by setting a pressure and varying the temperature or vice-versa. The E_c is also named the Seitz energy threshold. Then, total energy depositions above the Seitz energy threshold and within a volume defined by the critical radius of the fluid will nucleate a bubble), assuming a 100 % detector efficiency. The control of the thermodynamic parameters of the superheated liquid, results in a detector sensitive to WIMP nuclear recoils but (extremely) insensitive to electromagnetic interactions.

Chapter 3

The Compressionless Bubble Chamber

3.1 The Geyser concept

To detect very rare nuclear processes, B. Hahn and H. W. Reist, designed a variant of the bubble chamber using 20 litres of alcohol as superheated liquid (1974) [61]. Since the liquid produced small gas eruptions with each event, similar to the geothermal phenomenon, the detector was named Geyser. This experiment was successful in detecting the fission products from ^{238}U [61].

Geyser bubble chambers or compressionless bubble chambers are insensitive to all radiation except nuclear recoils like those induced by WIMP dark matter particle interactions. In this chapter, the compressionless bubble chamber filled with C_5F_{12} (C_5F_{12} Geyser for short) is described.

3.2 Geyser thermodynamics

The combination of gravity and temperature gradient permits the Geyser bubble chamber to achieve an almost continuously superheated state.

Bubble nucleation in a Geyser bubble chamber occurs when in the active volume, a particle deposits energy above the Seitz energy threshold (see section 2.3). Therefore, when the bubble forms, by the action of the Archimedes principle it rises through the liquid above (see figure 3.1). A vertical inverse thermal gradient allows lower temperatures to condense the bubble and the liquid to flow back to the active volume.

To suppress convection and thus maintain the inverse thermal gradient the chamber is divided into small chambers connected with thin capillaries.

Events can be identified by a pressure increase, by photography, or acoustic inside the superheated liquid.

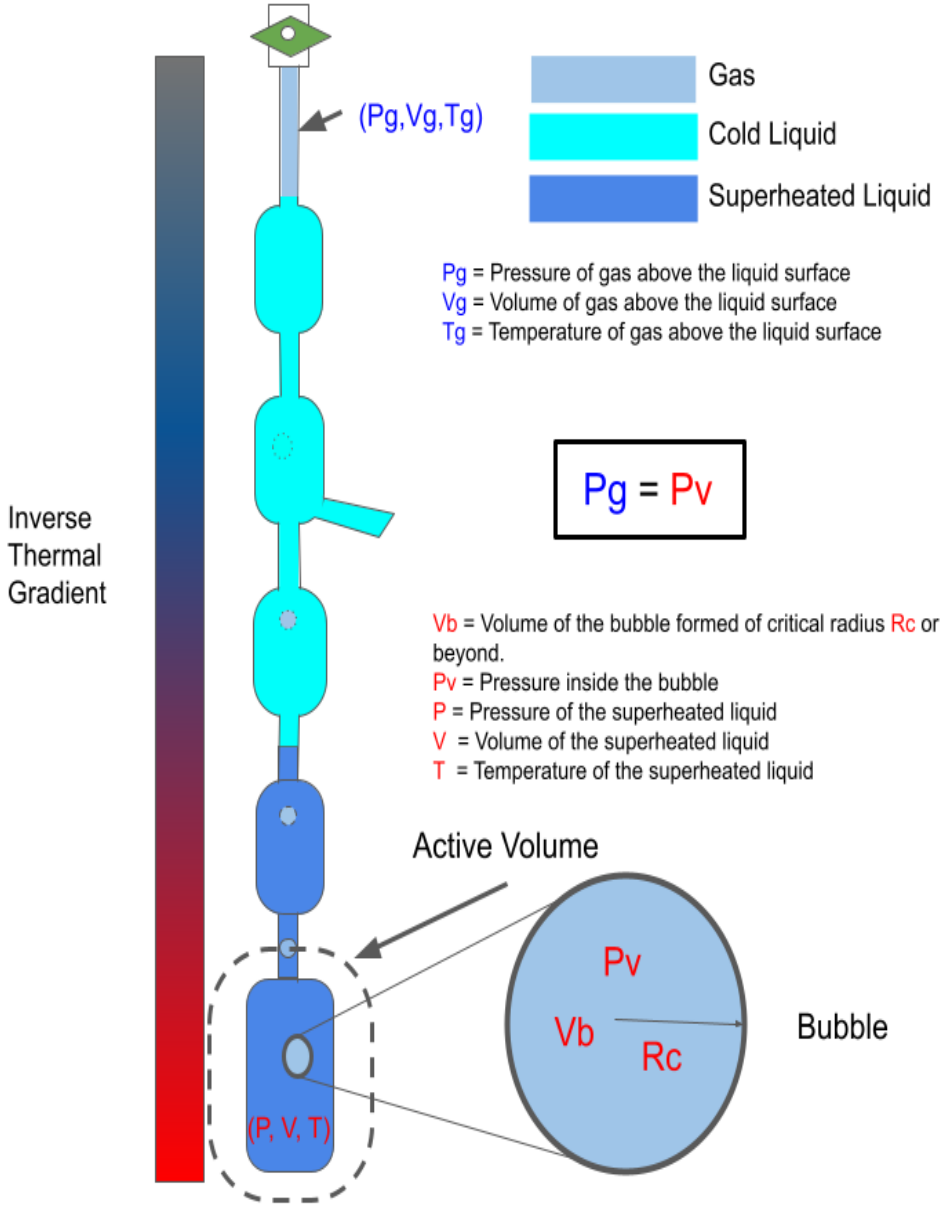

Figure 3.1: The pressure of operation of the Geyser bubble chamber is set by modifying the temperature of gas above the liquid surface (T_g). T_g is straightforward to control and measure.

3.2.1 Bubble formation

When a bubble of critical radius R_c is formed inside the Geyser chamber (see figure 3.1), the pressure inside the bubble (P_v), growing in size, is the same as the equilibrium vapor pressure (P_g) over the liquid surface [62]. Therefore, control over the temperature of the vapor above the liquid surface (T_g), sets the pressure of the Geyser bubble chamber. Together with the temperature of the superheated liquid (T), the Seitz threshold in a Geyser bubble chamber is well defined for each pressure and temperature of detector operation as shown in the figure 3.2.

In figure 3.1, under the assumption of a fixed amount of substance (n) in the gas phase above the liquid surface and enclosed in a volume (V_g), the general gas equation shows that $P_g \propto n/V_g$.

Then a decrease of (V_g) increases the pressure of the gas above the liquid surface (P_g) and vice versa. The value of V_g should be sufficiently small since it put limits to the maximum size a bubble can grow to. Furthermore, control over V_g is a requirement to maintain stability in the bubble chamber.

Notwithstanding, gaining direct control over the volume of the vapor pressure (V_g) is difficult to achieve, without affecting the self-recovery feature of a Geyser bubble chamber.

3.2.2 Thermodynamic cycle

Alternatively, the physical states of the thermodynamic cycle of Geyser, can be graphically represented in a phase diagram (figure 3.3). It consists of the following steps:

- (I) The liquid is initially at a temperature (T_o) and pressure (P_o). Increasing the temperature in the absence of a phase change, the temperature of vaporization T_v can be reached (black filled triangle 1 at figure 3.3).

- (II) Increasing the temperature beyond the saturation point along an isobar ($1 \longrightarrow 2$), the fluid passes from the saturated state to the super-

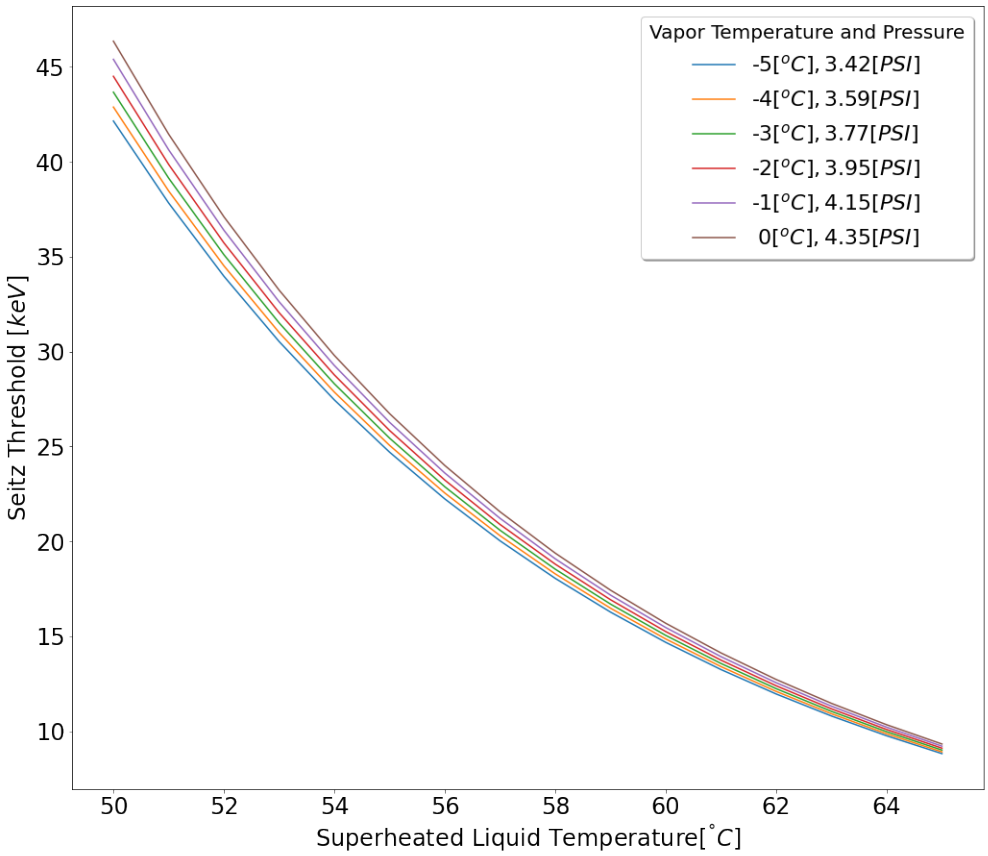

Figure 3.2: Calculated Seitz energy threshold at a given vapor temperature (and associated pressure), and superheated liquid temperature in a Geyser type bubble chamber filled with C_5F_{12}.

heated state. This state, also called metastable stays until an energy deposition breaks the equilibrium and leads to a phase change.

- (III) If an energy deposition happens, part of the liquid experiences a phase change ($2 \longrightarrow 3$). This depends on the amount of gas volume above the liquid surface. Otherwise, the phase transition will not happen.

- (IV) The fluid thermalized at a new temperature and pressure ($3 \longrightarrow 1$). Then, the fluid is ready for a new interaction if the pressure and temperature values have previously met the conditions of steps (I)-(II).

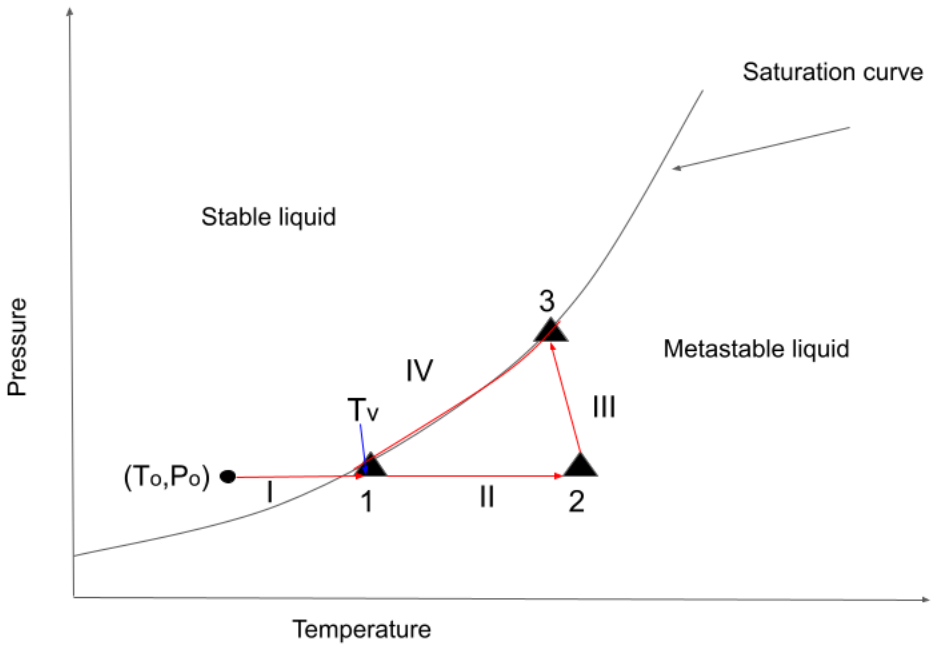

Figure 3.3: Geyser phase diagram. Initially the Geyser target liquid is at temperature T_0 and pressure P_0.

3.2.3 Limits of superheat

The lower limit of operation for a bubble chamber is the boiling temperature. On the other hand, the critical temperature T_c of the liquid is the theoretical upper limit where the liquid phase can no longer exist.

However, for a bubble chamber detector, the upper limit is set by the *foam limit*. This limit represents a temperature at which the probability of nucleation is so high, that bubbles immediately form in the liquid even in the absence of any external ionizing radiation [63]. By using the reduced Van der Waals equation of state, the foam limit can be estimated with the following equation:

$$p_R = \frac{8T_R}{3(v_R - 1/3)} - \frac{3}{v_R^2} \tag{3.1}$$

where $p_R = p/p_c$, $v_R = v/v_c$ and $T_R = T/T_c$. T is the temperature, p is the pressure, and v the molar volume. The indices R and c, denote the reduced and critical values respectively. If a saturated liquid at pressure p_R

is superheated, it will remain liquid until the minimum point of instability (metastable) is reached [64]. This point M can be found by setting

$$\left(\frac{\partial p_R}{\partial v_R}\right)_{T_R} = 0$$

whence

$$\frac{8T_M}{3(v_M - \frac{1}{3})^2} = \frac{6}{v_M^3} \tag{3.2}$$

where T_M is the metastable temperature, and v_M the metastable volume. Substituting the equation 3.2 into equation 3.1 and solving for a given metastable pressure (p_M),

$$p_M = \frac{1}{v_M^2}\left(\frac{2(3v_M - 1)}{v_M - 3}\right) \tag{3.3}$$

combining equations 3.2 and 3.3, T_M can be given as function of p_M. When both equations are solved simultaneously, the reduced temperature T_R can be computed and the temperature T associated with this value is interpreted as the foam limit.

The case for C_5F_{12}

The lower limit of superheat for a bubble chamber filled with C_5F_{12} is given by the boiling temperature ($T_{boiling} = 29$ °C).

The foam limit can be deduced from the critical thermodynamic parameters of C_5F_{12}. Those are taken from [65] ($p_c = 297.04$ [psi], $T_c = 148.75$ °C and $v_c = 0.48\ m^3/(kg \cdot mol)$) and are used in the equations 3.1 and 3.3. Assuming a value of $p = 35$ [psi] as the bubble chamber operating pressure, the foam temperature is:

$$T = 96.24\ ^\circ C \tag{3.4}$$

The C_5F_{12} Geyser chamber was operated at temperatures far below this limit so there should be no thermodynamic limitations of the chamber stability for the data studied here.

3.3 C_5F_{12} Geyser

3.3.1 Description

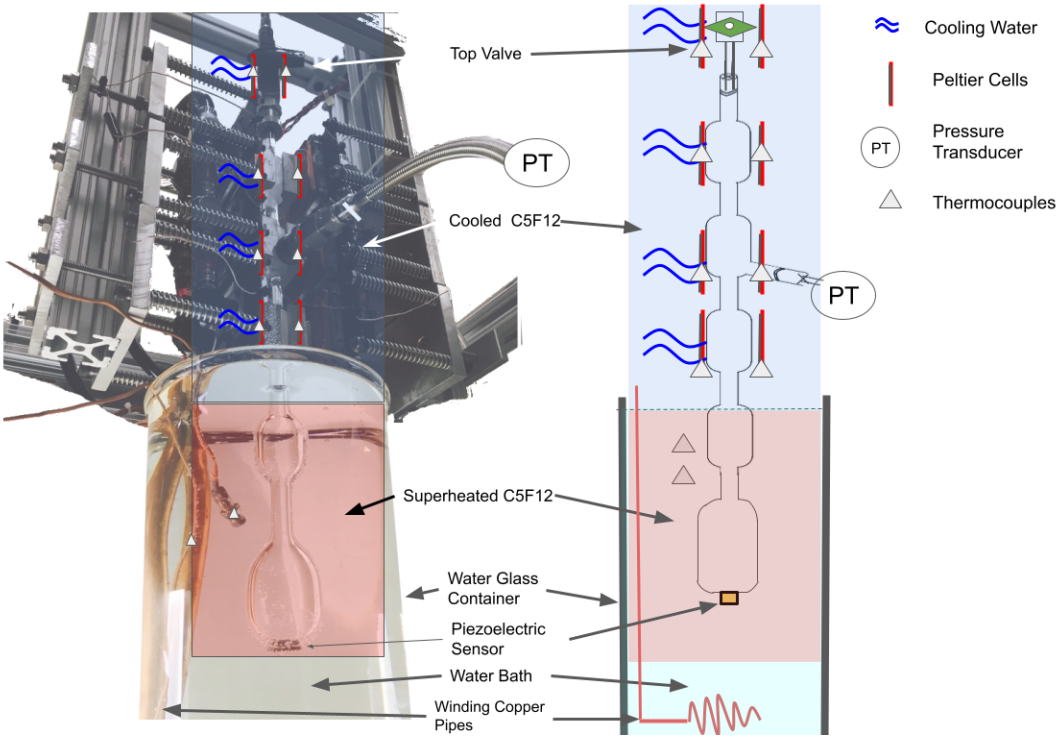

Figure 3.4: Setup of the C_5F_{12} Geyser main parts.

A Geyser bubble chamber filled with C_5F_{12} (i.e. fluorocarbons [1]) is advantageous for the following reasons: The large fraction of fluorine is excellent for WIMP detection given its large spin-independent enhancement factor for nuclear recoils (see table 1.1). The PICO collaboration has demonstrated the use of fluorocarbons (C_3F_8, CF_3I) as target fluids by setting world-leading limits on the spin-dependent WIMP-proton couplings [44]–[46]. Additionally for the target material (C_5F_{12}) studied here, the detector can be easily scaled and is easy to superheat. For instance, a C_5F_{12} Geyser bubble chamber sensible to 10 keV nuclear recoils, requires a superheated liquid temperature of 64 ^{o}C and a top gas temperature of -4 ^{o}C.

The C_5F_{12} Geyser in figure 3.4 is constructed following the design of an

[1] Fluorocarbons are compounds with the formula C_xF_y, i.e., they contain carbon and fluorine atoms.

alcohol-based Geyser operated at the University of Alberta in 2013 [58]. The C_5F_{12} is contained in a quartz vessel constituting of five bulbs oriented vertically as shown in figure 3.4.

Compared to glass the quartz material of the Geyser vessel reduces the backgrounds due to smaller traces of radioisotopes. An additional measure to reduce backgrounds due to particulates or dust [2] is taken by cleaning the quartz container with distilled water, acetone, and an aqua regia solution.

An inverse temperature profile is kept in the chamber by submerging the lowest two bulbs in a heated water bath. The lowest bulb is slightly larger than the others and acts as the volume for particle detection (the lowest bulb is labeled as superheated C_5F_{12} in figure 3.4).

The top three bulbs and the top valve region (labeled cooled C_5F_{12} and top valve in figure 3.4) are cooled to a constant temperature following an inverse gradient (see figure 3.11).

Therefore, when a bubble forms in the superheated C_5F_{12} it rises through the top chambers (cooled C_5F_{12}) and top valve where the lower temperatures will cause it to condense.

Events in the C_5F_{12} Geyser are registered primarily by the pressure change in the superheated C_5F_{12} using a pressure transducer. Also, piezoelectric sensors can be used for acoustic discrimination between alphas and nuclear recoils (not used in this analysis) as in the PICO bubble chambers. A camera allows counting of bubbles and reconstruction of the location of the nucleation (also not used here).

3.3.2 Design properties

The main property of the Geyser chamber is its self-regulating operation principle of work, which does not require external intervention to return to an active state. Instead, the system is actively cooled at the top and heated at the bottom, creating an inverse thermal gradient to sustain the superheated state. As with any other superheated liquid technology for WIMP and radiation detection, the C_5F_{12} Geyser can change the active liquid according to

[2] An identified source of spontaneous nucleations.

the physical models of WIMPs to explore as well be scaled without further complications in the general design.

Unlike a traditional bubble chamber, a Geyser type chamber can be compressionless or not pressure controlled. This fact makes it an affordable solution in terms of construction, mechanical design (no moving parts) and safe operation. The absence of a buffer liquid in a Geyser type bubble chamber leads to a type of detector with no complications from buffer-active liquid chemistry. If a stable operation at low threshold (O(keV)) can be demonstrated, this kind of chamber can be considered as an alternative design for the future PICO bubble chamber program. However, the Geyser bubble chambers that have been constructed did not reach Seitz thresholds at O(10) keV and stable operation.

Being able to thermally control the superheated region (superheated C_5F_{12}, figure 3.4) and the vapor region is the main idea of the compressionless bubble chamber operation.

To improve thermal isolation at the cooled C_5F_{12} region, a custom styrofoam housing for the top valve above the Geyser was constructed as shown in figure 3.5. To avoid heat exchange between the top Geyser bulbs and the water bath, a circular styrofoam lid was added to the top of the glass water thermal bath.

Another source of instability and anomalous nucleation is the liquid-glass interface. Here, it is likely that the liquid boils. Geyser operation in 2018 showed visual evidence of continued bubbles at the glass walls. This came to overwhelm the cooled C_5F_{12} region contributing to unstable operations and high energy thresholds.

To stop the nucleation, a manually operated pressure control was connected to the Geyser. Since this device had limitations in controlling the wall nucleation, alternative ways to control it were investigated.

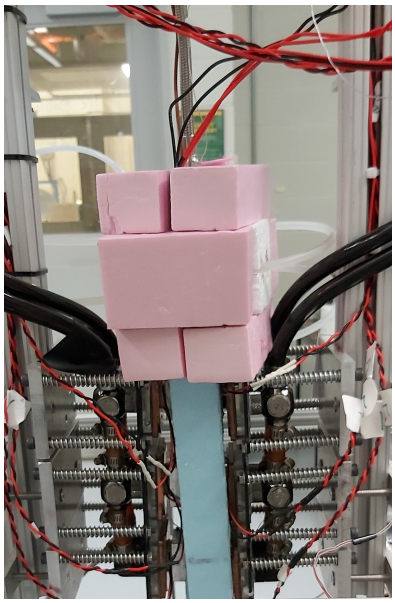

Figure 3.5: The pink and blue styrofoam make up an enclosure to the Top valve region (see figure 3.4). This avoids thermal exchange with the surroundings.

3.3.3 Volume control of the liquid

As the gas volume above the cold liquid C_5F_{12} is sharing a fixed volume with the whole liquid (see figure 3.6) any change of the liquid phase thermodynamic properties (pressure, temperature, volume) affect the gas. As a consequence, the exact control of the gas volume affects the energy threshold of the C_5F_{12} Geyser by changing the gas pressure.

A small gas volume above the cold liquid limits the size of any bubble because there is not enough room in the container for the bubble volume to grow.

By setting the gas volume (V_g), the wall bubble size is affected since they could no longer grow larger. Then, with an exact amount of V_g set, the continuous boiling on the walls can be stopped.

To control the bubble growth in the Geyser by the control of V_g, a hydraulic system was constructed. It uses elements from the hydraulic system design of the PICO-2L [44] experiment.

The hydraulic system (see figure 3.7 and 3.8) uses a pump (Micropump model GAF-T23-DEMSE), two hydrin diaphragm pressure accumulators (Parker

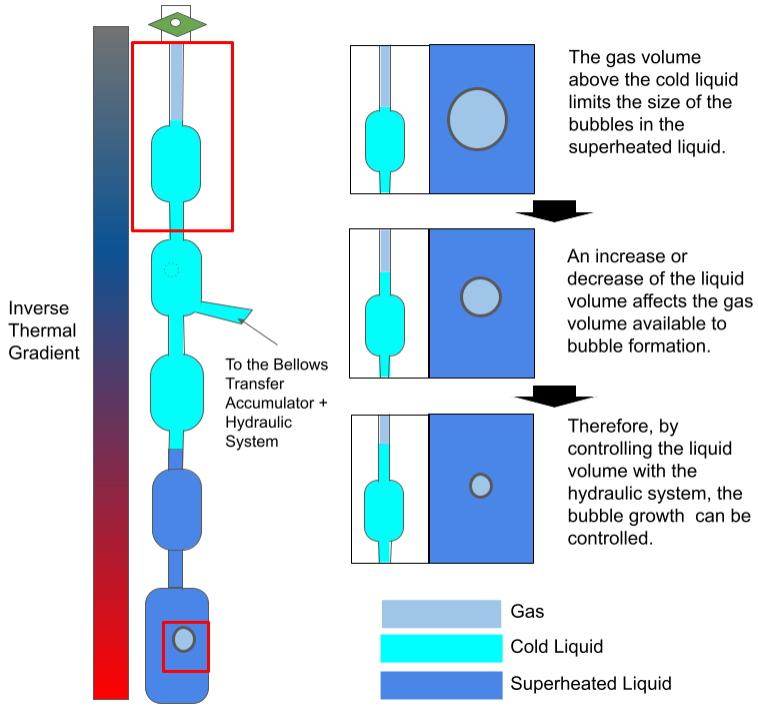

Figure 3.6: Schematics of the Geyser bubble size as a function of the gas volume above the liquid.

Model AD100A21T9) and a series of valves to control the hydraulic fluid (mineral oil) released at the output.

The pressure is monitored by pressure transducers (OMEGA PX319-300A-5V) at the ends of the two diaphragm accumulators and the hydraulic system output.

The hydraulic system components are controlled and monitored by a National Instruments CompactRIO (NI-cRIO 9066), which communicates with the data acquisition systems and storage via a LabVIEW VI (Virtual Instrument). This interface allows controlling the amount of active liquid in the Geyser.

The hydraulic system can also be used as a pressure cycle device as in PICO-2L experiment. However, the C_5F_{12} Geyser mechanical design is not optimal for this working condition.

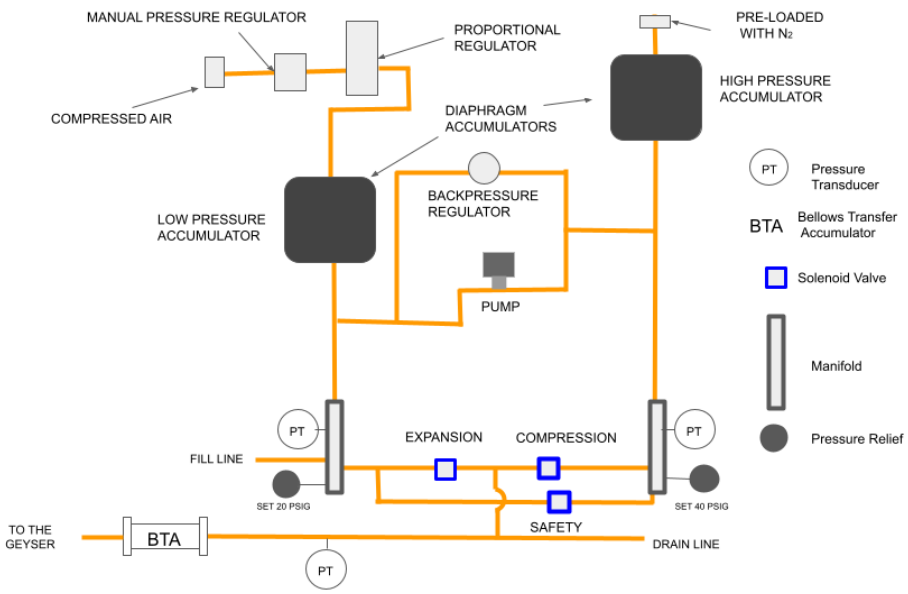

Figure 3.7: Schematics view of the hydraulic system.

Figure 3.8: Photograph of the hydraulic system.

3.3.4 Cooling Control and Data Acquisition System

The first and the second-lowest Geyser bulb are heated by a water bath. Winding copper pipes fed with water from a heater/cooler (Polyscience AD15R-30-A11B) are in charge of this heating (see figure 3.9).

The case for the cooling of the top three Geyser C_5F_{12} bulbs (cooled C_5F_{12}) and top valve region is as follows. Eight thermoelectric Peltier cells (TEC1-12710HTS), powered by a 12 V DC supply are cooling this region. The voltage is controlled with an Arduino DUE board (based on the Atmel SAM3X8E microcontroller). The Arduino DUE shown in figure 3.10, has 54 digital input/output pins, of which 12 can be used as PWM (Pulse-Width Modulation) outputs.

The PWM ports 6, 7, 8 and 9 are connected to solid-state relays which are connected to the thermoelectric Peltier cells accordingly. Water-cooled heatsinks are used to cool the Peltier cells as well as to refrigerate the system. Those are mounted on both sides of the three top Geyser bulbs and in the top valve region. Temperatures are recorded by 8 J-Type thermocouples located close to each of the top three bulbs of the Geyser and the Top valve region [3]. Two additional J-Type thermocouples are immersed in the thermal water bath to monitor the temperature of the superheated C_5F_{12}. The thermocouples are represented by smalls triangles in figures 3.9 and 3.11.

A pressure transducer (Omega PX319-100AI) detects pressure spikes and monitors the pressure. The pressure transducer is represented by letters PT enclosed by a circle in figures 3.9 and 3.11.

The thermocouples and the pressure transducer are connected to the same Arduino DUE board.

The thermal data acquisition on the Arduino records temperature (sampling rate: 1 Hz) and pressure data (sampling rate: 10 Hz). It is transmitted from the Arduino using a serial interface protocol to a local computer where it is decoded using the twisted-Python framework for event-driven programming.

Finally, the data is stored together with a timestamp in a MySQL database

[3]The thermocouples are glued with epoxy onto an aluminum heat spreader in contact with the glass.

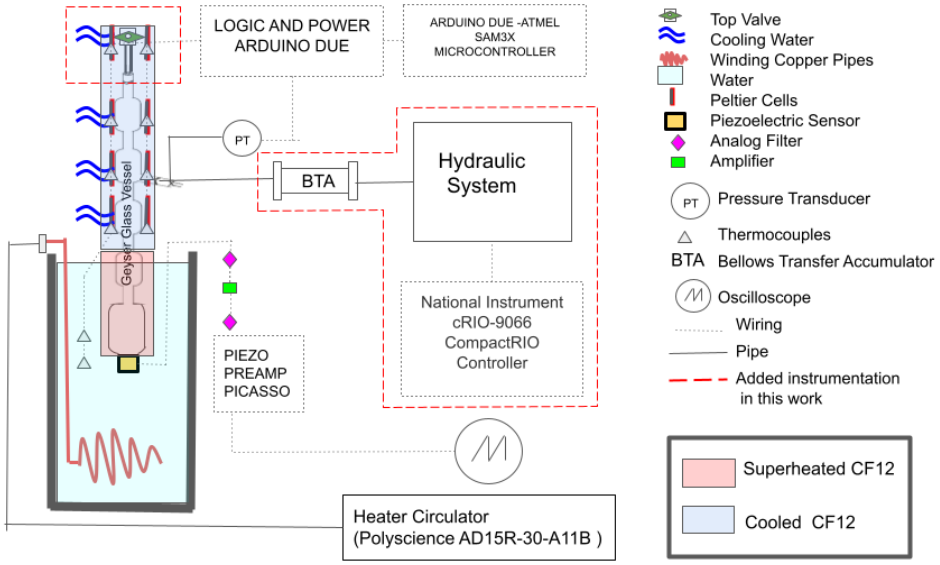

Figure 3.9: Schematic of the C_5F_{12} Geyser and the hydraulic system.

on the same computer.

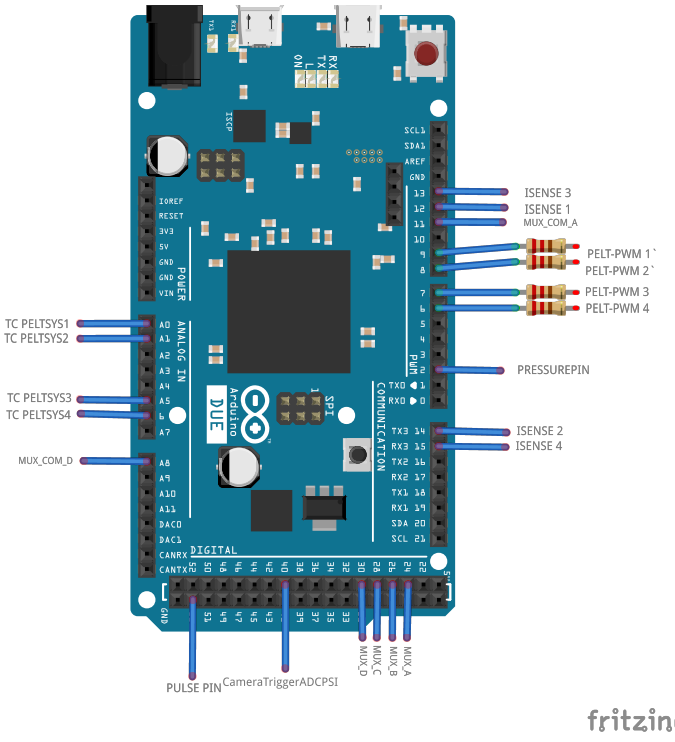

Figure 3.10: Arduino pinout schematics. The diagram was produced using the software Fritzing. Names around the pins are used for reference in the Arduino compiled code.

3.3.5 Operating conditions

The Geyser top three bulbs and top valve temperatures are controlled using the Arduino DUE electronics setup. The range of temperatures that can be set depends on the Arduino DUE input voltage and the cooling water flow and temperature.

A PHP local web server communicates with the Arduino DUE through an HTML page that receives as a human-readable number the temperature value to be set in degrees Celsius.

Meanwhile, the two bottom bulbs (i.e. the superheated C_5F_{12}) temperature depends on the heater/cooler circulator set temperature (shown in figure 3.9 at the lower center). The main limitation for reaching a temperature above 57

^oC is the fast water evaporation of the water bath [4].

On the other side, the maximum pressure the Geyser can be operated is set by the ultra-torr fittings between the glass to the top valve boundary. According to the fabricator of these fittings, pressures above 30 psi lead to a leak in the chamber.

Figure 3.11 shows the temperature conditions set for each of the Geyser bulbs (except the second from the bottom) as well as the range of pressure, registered by the pressure transducer.

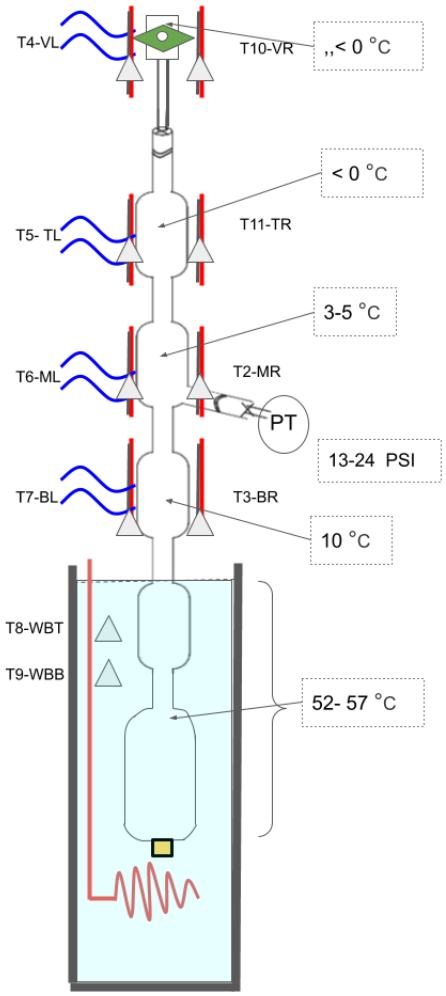

Figure 3.11: Typical thermodynamic parameters of the C_5F_{12} Geyser operation. The plain text indicates reference notation for identification purposes for the MySQL database where temperature and pressure data are saved. Absent labelling can be cross-checked in figure 3.9 (not included here for clarity).

[4]The water bath container had to be refilled over periods of 10 min.

Chapter 4

Data Analysis and Simulation of the Superheated C_5F_{12}

A compressionless bubble chamber filled with C_5F_{12} is optimized for detecting nuclear recoils in the keV region. This means neutrons with energies between keV and MeV.

Because neutrons are electrically neutral, they can reach nuclei without being repelled by the Coulomb interaction and scatter elastically of the whole nucleus imitating the coherent nuclear scattering of WIMP dark matter interactions.

When a flux of neutrons passes through a superheated liquid(e.g. C_5F_{12}), a percentage of them interact with the active liquid by elastically scattering on the nuclei inside the molecules and ejecting these nuclei with various velocities. The ejected charged nuclei interact with the electrons of the medium and eject them from their electron orbitals. Depending on the energy, the ejected electrons lose their energy through lengths of cm. If this process is localized and energetic enough to meet the conditions explained in section 2.1, the deposited energy generates a bubble.

An understanding of the neutron scattering in the experimental environment of the Geyser is important in the interpretation of results and design of scaled prototypes for WIMP dark matter searches.

In this chapter, the events (bubbles) produced in the superheated C_5F_{12} due to an AmBe neutron source are presented (see next section). The pressure and temperature under which the neutron data were taken are used for calculating

the number of events (bubbles), Seitz thresholds, live-time, dead time, event rates and efficiency of the Geyser.

Those results are compared and validated with a Geant4 Monte Carlo [66] simulation of the neutron scattering under the same conditions at which the data was taken with superheated C_5F_{12}.

4.1 AmBe Neutron source

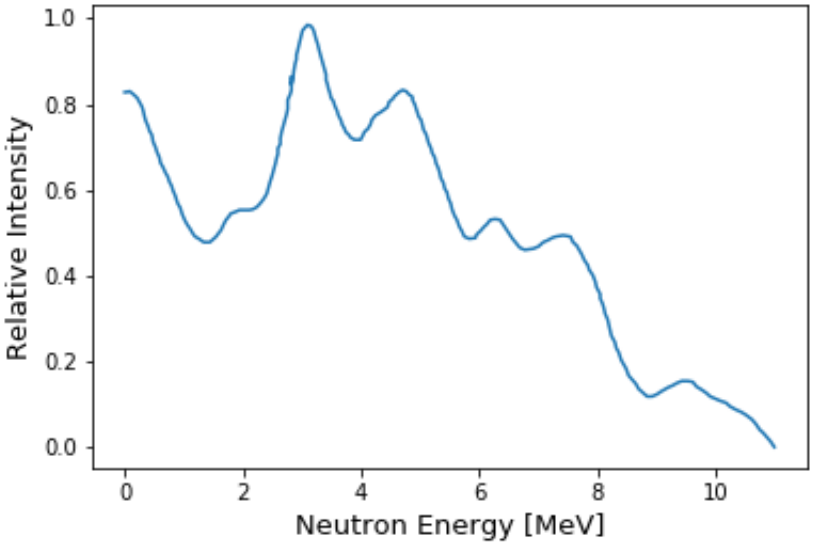

Figure 4.1: The neutron energy spectrum produced by an AmBe neutron source [67]. The neutron energy ranges up to 11 MeV.

Neutron sources, which consist of a mixture of ^{241}Am and ^{9}Be are referred to as AmBe sources. The ^{241}Am produces α particles with an energy of 5.48 MeV and a half-life of 432.2 years.

The α particle emitted by ^{241}Am can be absorbed by the ^{9}Be target, which will then decay into ^{12}C through neutron emission, such as:

$$\alpha + {}^{9}\mathrm{Be} \longrightarrow {}^{1}\mathrm{n} + {}^{12}\mathrm{C} \qquad \mathrm{Q} = 5.701 \text{ keV} \tag{4.1}$$

For this study, the documented AmBe spectrum from reference [67] is used. The source used in the Geyser experiment, it was made by Eckert Ziegler Isotope Products, Inc. (AM241SNA02). It consists of a homogeneous mixture of

americium oxide and beryllium metal within a double stainless steel encapsulation, each layer with a thickness of 0.8 mm [68]. The source strength was documented to be 305.6 ± 4.9 neutrons per second on the 17th of Jun 2015 [68].

4.2 Monte Carlo Neutron Modelling

Neutron scattering information for design purposes and analysis of radiation detectors can be obtained from Monte Carlo neutron transport calculations. The two codes used most often are MCNP [69] and Geant4 [66]. These codes describe the neutron interaction with materials using databases of neutron scattering cross-sections measured experimentally [70].

Geant4 (GEometry ANd Tracking) [66], is a software toolkit developed at CERN that performs Monte Carlo simulations and particle tracking. It is widely used not only in particle physics but also for cosmic-ray, radiation and medical therapy simulations [66]. Programmed in C++, Geant4 allows users to define the geometry of the experimental setup. The main components of the Geant4 simulation of the compressionless bubble chamber are matching the experiment with a precision of 1 millimeter (measurements were taken in situ with vernier calipers). The simulation includes all main components: the quartz water bath container, water, and the superheated liquid (see figure 4.2). Detector materials are defined using the standard chemical formula for water (H_2O), air (80 % nitrogen, and 20 % oxygen), quartz (SiO_2) and perflenapent (C_5F_{12}).

The AmBe source is modeled as an isotropic neutron point source. The neutron energy spectrum was generated using the Geant4 general particle source (GPS) package using the weights from the spectrum shown in figure 4.1.

The electromagnetic interactions are modeled in Geant4 using the *Low Energy EM* package. On the other hand, the *NeutronHP* package is invoked within Geant4 to model the interaction and transport of neutrons within the detector components.

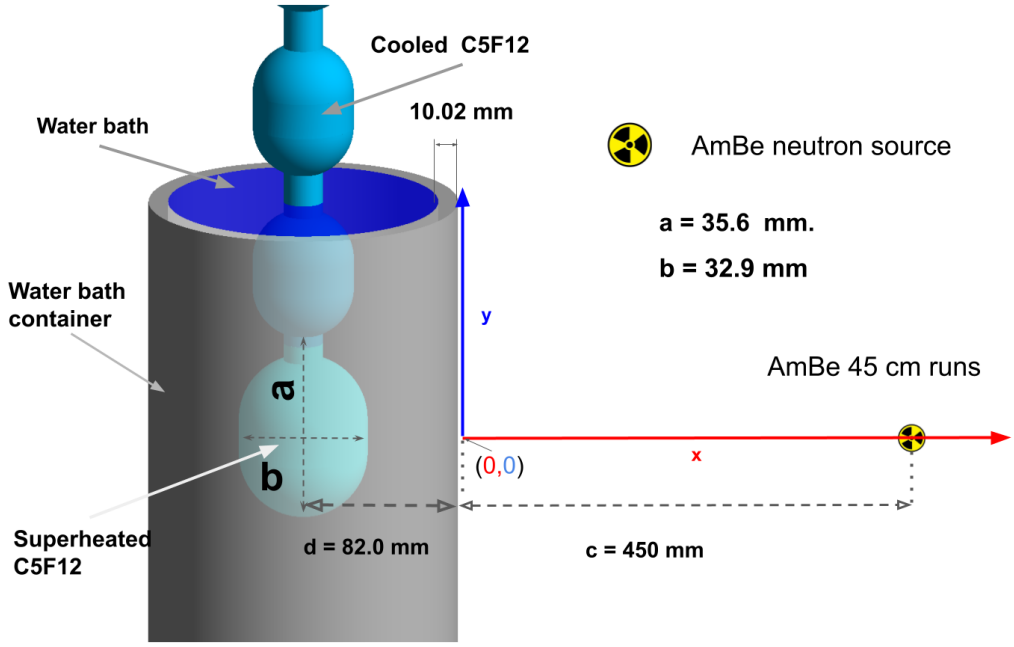

Figure 4.2: The Geant4 representation of the Geyser geometry using the Qt visualization driver. The cold C_5F_{12} is a distinct volume from the active volume (superheated C_5F_{12}).

4.2.1 AmBe neutron simulation output

The output from the Geant4 simulations is saved in plain text. The plain text file contains the following information:

- Event identifier.
- The amount of energy deposited inside the superheated C_5F_{12}.
- Atomic code of the nucleus that takes part in the interaction. The options are carbon and fluorine.
- The 3D spatial coordinates of the event.
- The primary neutron energy from the AmBe source.

The effect of multiple-scattering neutron events is not taken into account in this analysis. Instead, all events are treated as single scatters without

distinction of the type of the associated nucleus recoiled in the superheated C_5F_{12}.

4.3 Neutron Data Analysis

4.3.1 The Data

Between 2014 and 2018, the Geyser was operated. The first operation was used to learn how to operate the chamber and improve data taking. After a second run after an aqua regia cleaning of the Geyser, stable operation was achieved in 2018. Several runs were taken to assess the response of the superheated C_5F_{12} to neutrons and background events. Initial runs did suffer from repeated boiling. Later, even when using a manual compression valve to control the amount of active liquid, the amount of runaway bubbling was not properly controlled.

The first step of this analysis was to explore the pressures and temperatures at which the data were taken. Only complete and well documented runs were analyzed.

For the pressure and temperature values of all runs, the Seitz energy threshold associated with each corresponding pair of values is calculated using the PICOcode software framework. PICOcode is used as a basis for parameter calculation of the PICO bubble chamber program for WIMP dark matter searches [44]–[46].

Only runs with events that have thresholds below 1000 keV are taken into account. Runs with thresholds consistently above 1000 keV are mostly runs where the Geyser was not functioning as intended. Overall 13 good runs were selected for the whole analysis of this work and two dataset categories were defined (see also table 4.1):

- **Background runs**, correspond to data taken without a radioactive source. Runs were taken in three periods of time: 2014, 2016, and 2018. 2014 and 2016 data were discarded due to Seitz energy thresholds above 1000 keV. All 2018 runs were analyzed.

Feature of the datasets	**AmBe 45 cm runs**	**Background runs**
Date (Runs)	2018-03-21 (471, 472, 473) 2018-03-22 (499)	2018-02-22 (138, 139) 2018-02-24 (146-153)
Average pressure $[psi]$	22.69 ± 4.76	23.53 ± 4.85
Average temperature $[^oC]$	56.95 ± 7.54	53.36 ± 7.30
Total live-time $[hours]$	2.45 ± 0.03	9.42 ± 0.01
Average Seitz energy threshold $[keV]$	248.87 ± 15.77	719.41 ± 26.82
Counts $[N]$	96 ± 10	37 ± 6

Table 4.1: Description of the properties of the Geyser datasets considered in this analysis.

- **AmBe 45 cm runs**, correspond to data where the AmBe source was located 45 cm away from the C_5F_{12} Geyser water container. The location of the AmBe source is illustrated in figure 4.2.

4.3.2 Event reconstruction

As a preparatory step in the analysis, the raw data from the experiment is exported from the C_5F_{12} Geyser MySQL database. Each run from the raw data is organized in event records. Every event record has a corresponding set of all the thermocouple and pressure transducer values at a given timestamp as indicated in figure 3.11. Furthermore, an analysis is performed using the JupyROOT environment for each run. JupyROOT is a software layer that integrates the Jupyter-Python language and the ROOT software framework [71]. Candidate events that fulfill the data quality conditions of section 4.3.1 are defined as follows.

4.3.3 Event definition

The rise of pressure inside the Geyser is caused by the appearance of a bubble (see orange points in figure 4.3). These correspond to the pink zones in figure 4.3. An event is complete once the pressure in the Geyser has reached a lower value again. The end of a set of typical events can be seen in figure 4.3 where the pink area ends (or green points at the same figure).

Parameter	**AmBe 45 cm runs** 2018-03-21 (471, 472, 473) 2018-03-22 (499)	**Backgrounds runs** 2018-02-22 (138, 139)	**Backgrounds runs** 2018-02-24 (146-153)
Height	1	0	0
Prominence	1	0.95	1
Distance	5	100	30

Table 4.2: Values of the peak finder algorithm parameters used for this analysis.

To identify the highest and lowest pressure value (extreme values) that defines the start and end of a bubble appearance respectively, a peak finder algorithm is applied to the pressure data using the open-source *scipy-signal-findpeaks* python library. This algorithm finds all extreme values by a simple comparison of neighboring values. The peak finder algorithm parameters such as height, prominence and minimum distance are optimized empirically. A table of the parameters used is shown in table 4.2.

Better identification of the extreme values is achieved when the peak finder algorithm is applied to the pressure signal that results from applying the *numpy.gradient* of 4th order [1]. The *numpy.gradient* is computed using central differences in the interior (equation 4.2) and first differences at the boundaries (equation 4.3). This means that in the interior it is computed as

$$\delta_h[f](x) = f(x + \frac{1}{2}h) - f(x - \frac{1}{2}h) \qquad h = 1.0 \tag{4.2}$$

and at the boundaries,

$$\Delta_h[f](x) = f(x + h) - f(x) \tag{4.3}$$

The associated timestamp of the aforementioned 4th derivative helps to locate the pressure extreme values more cleanly (see figure 4.3).

Once the start of each event is located in the pressure profile (identified as orange dots in figure 4.3), an average of the ten previous pressures (green

[1] 1st, 2nd and 3rd order derivatives were not enough efficient to identify the peaks

zones in figure 4.4) is obtained. Likewise, an average of the corresponding ten temperatures of the superheated-C_5F_{12} (green zones in figure 4.5) is made.

These two average values, pressure and temperature, serve as parameters to the PICOcode for calculating the Seitz energy threshold of that particular event (see figure 4.6).

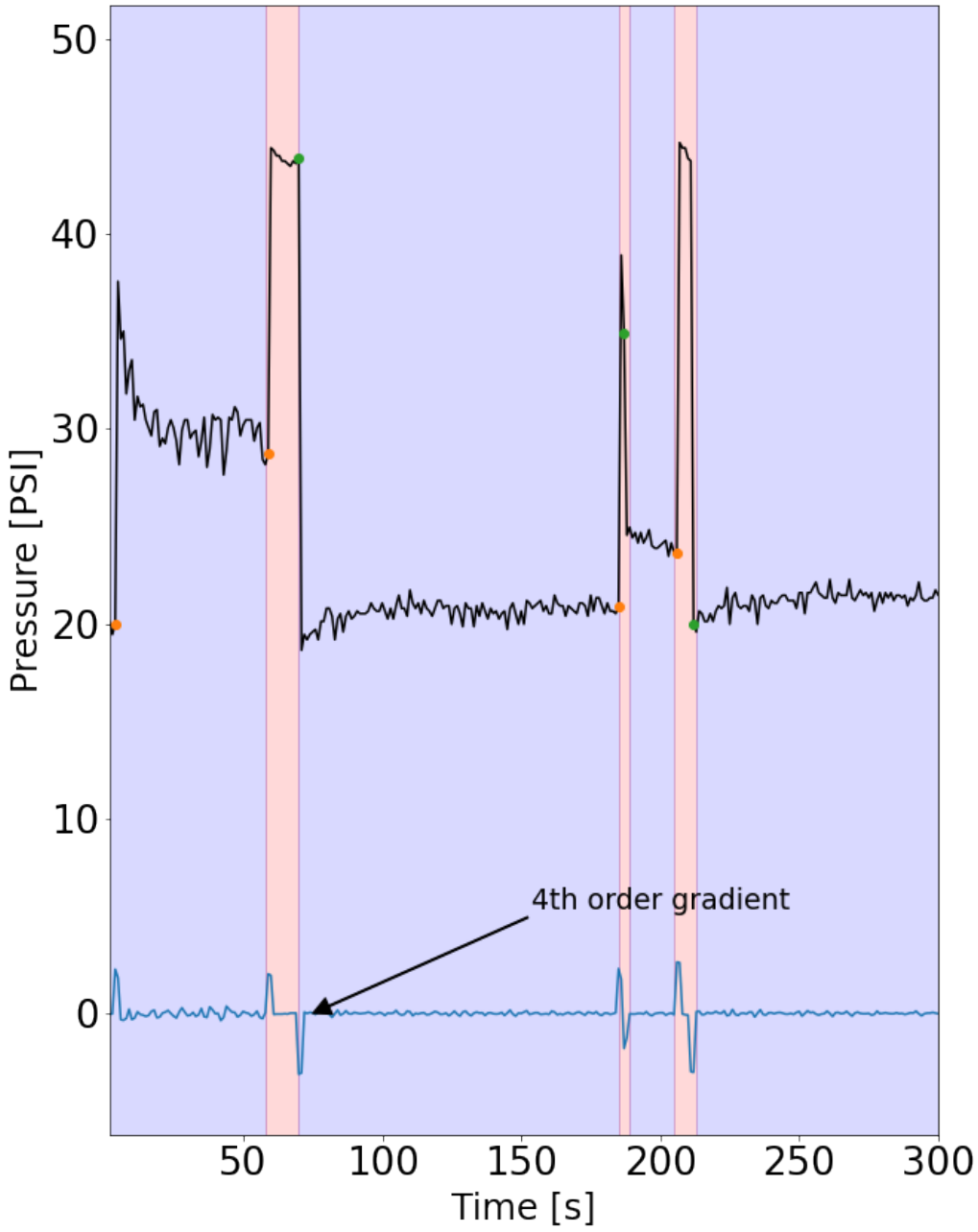

Figure 4.3: Event pressure pattern during run 499 in the C_5F_{12} Geyser. The occurrence of an event is marked by the transition from purple to pink. The purple zones are live-time, while the pink ones are dead time.

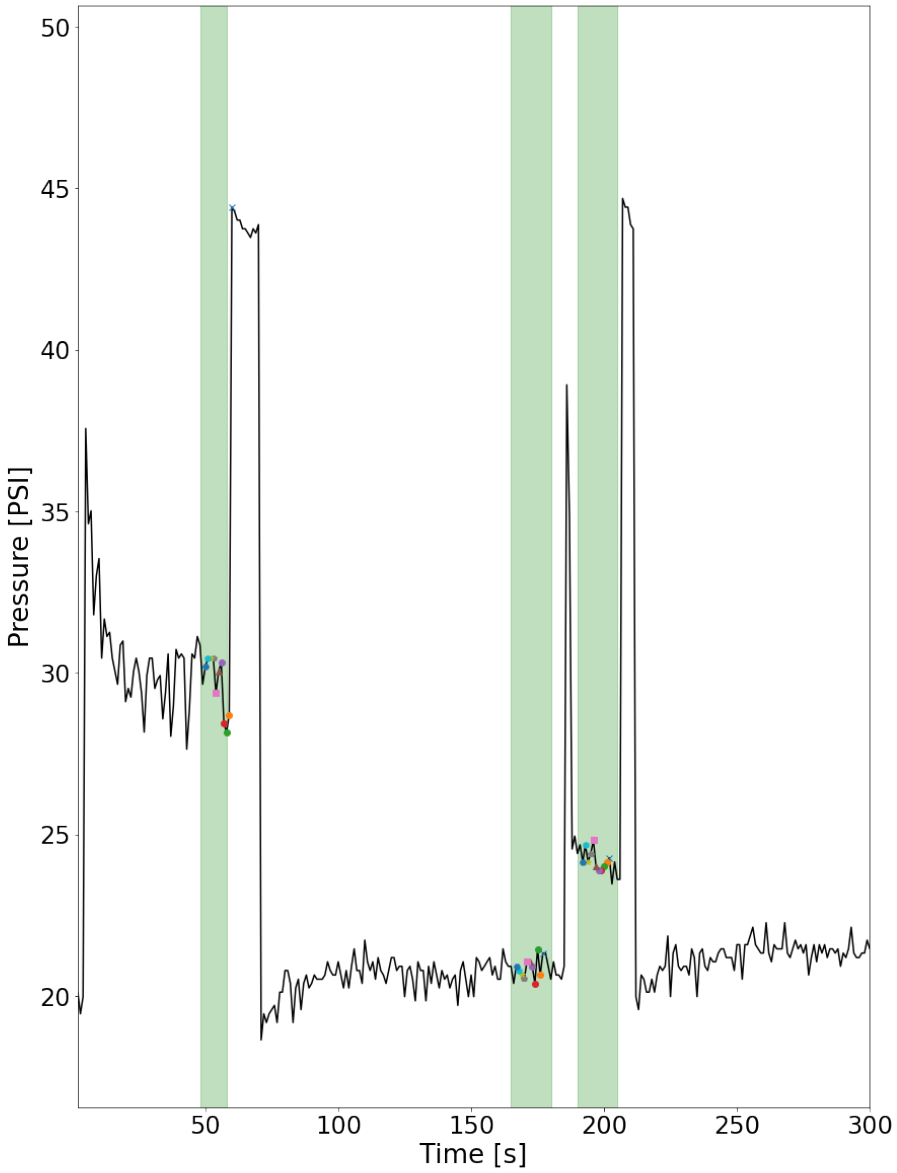

Figure 4.4: Event definition showing a period of run 499. The green zones correspond to the ten pressure data points (colorful dots inside green zones) before the dead time zones shown in figure 4.3.

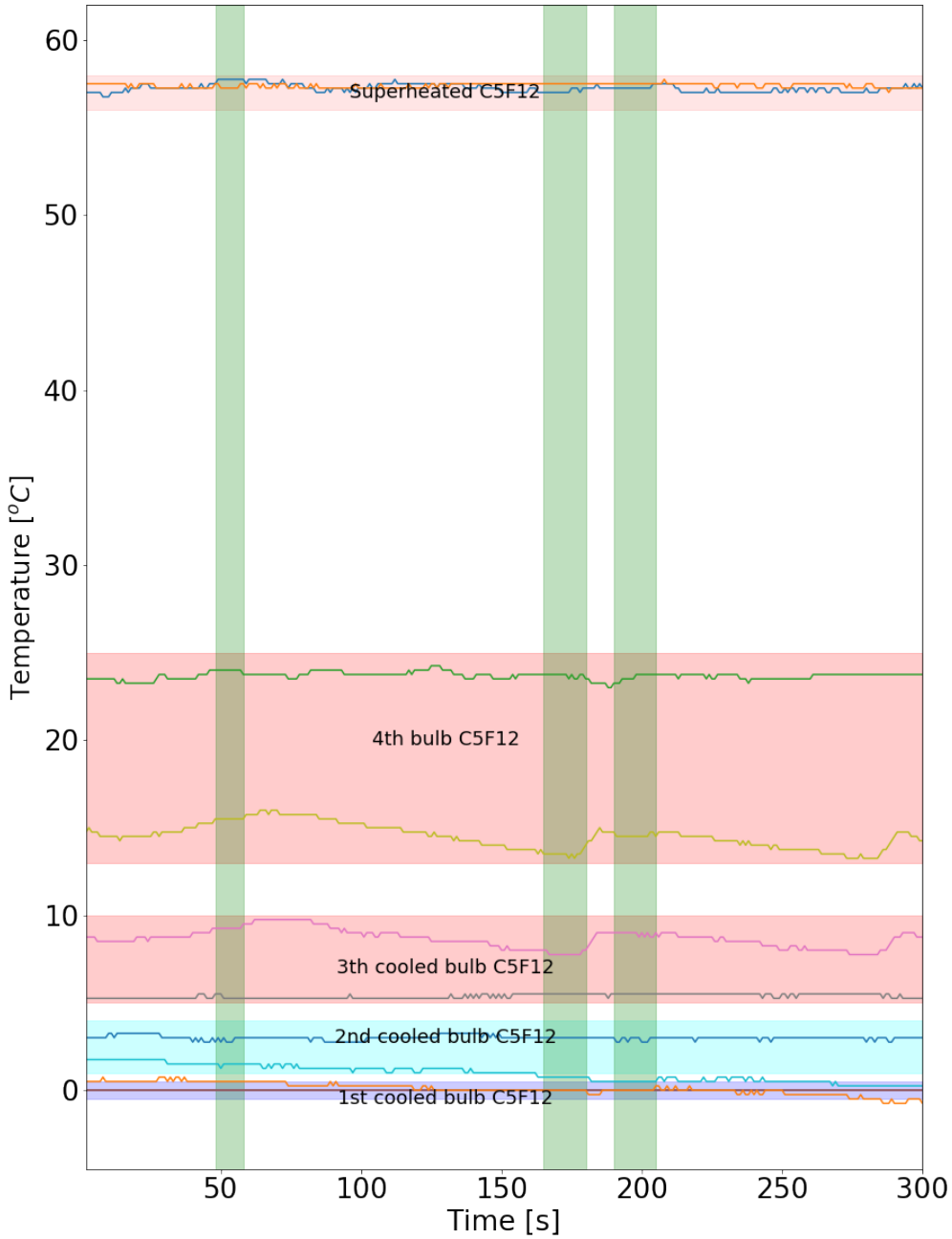

Figure 4.5: Temperature of the different Geyser bulbs for the same duration of run 499 shown in figures 4.3 and 4.4. The superheated C_5F_{12} temperature is assumed to be in thermal equilibrium with the water bath.

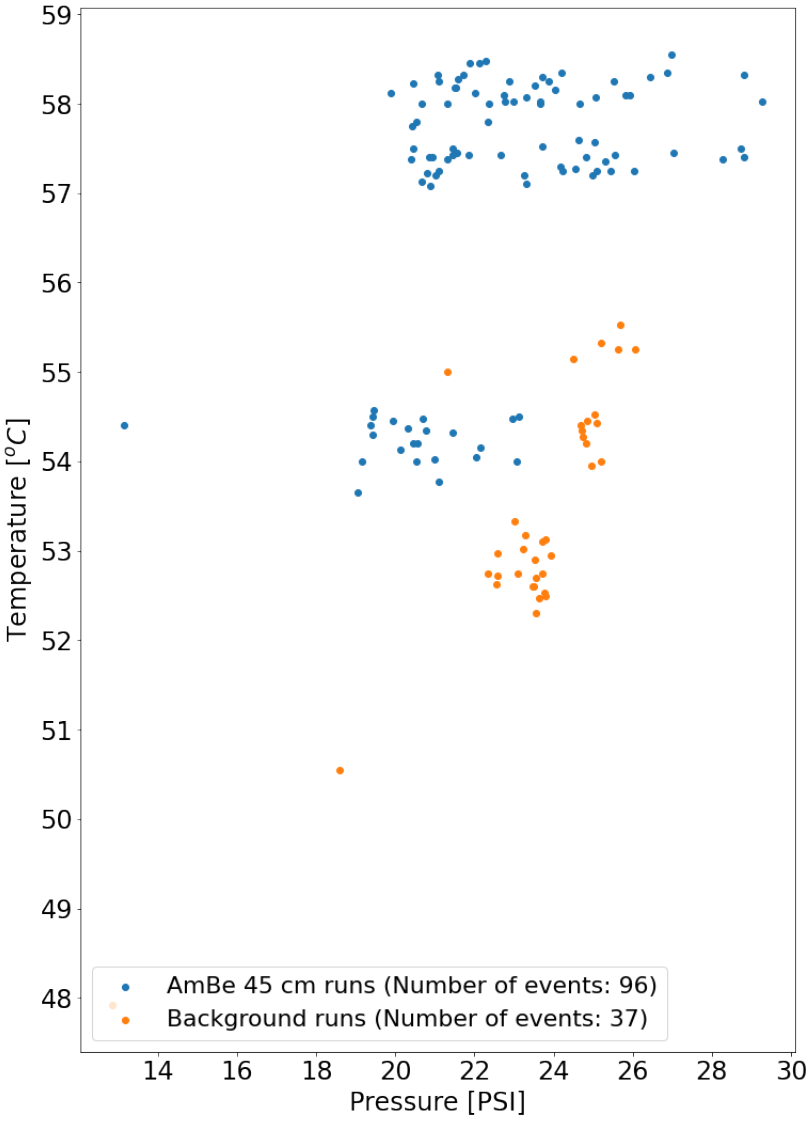

Figure 4.6: Pressure and temperature values for each of the Geyser events.

4.4 Seitz energy threshold, live-time, and dead time

The Seitz energy threshold is calculated for all identified events in figure 4.6 using the PICOcode. These correspond to the *AmBe 45 cm* and *Background* datasets.

In figure 4.7, the Seitz threshold of the *AmBe 45 cm* is histogrammed for all detected events. Is worthwhile to note the minimum Seitz energy threshold reached by the detector is 72 keV. Similarly, in figure 4.8 the Seitz energy thresholds for detected events are shown for the *Background* dataset. In the counting of figures 4.7 and 4.8, Poissonian errors are assumed.

The live-time of the C_5F_{12} Geyser is the time during which the detector is superheated, stable and taking data. The accumulated live-time of the runs contained in the *AmBe 45 cm* and *Backgrounds* runs datasets are plotted as a function of the Seitz threshold in figures 4.9 and 4.10 respectively. The same information is summarized in table 4.1.

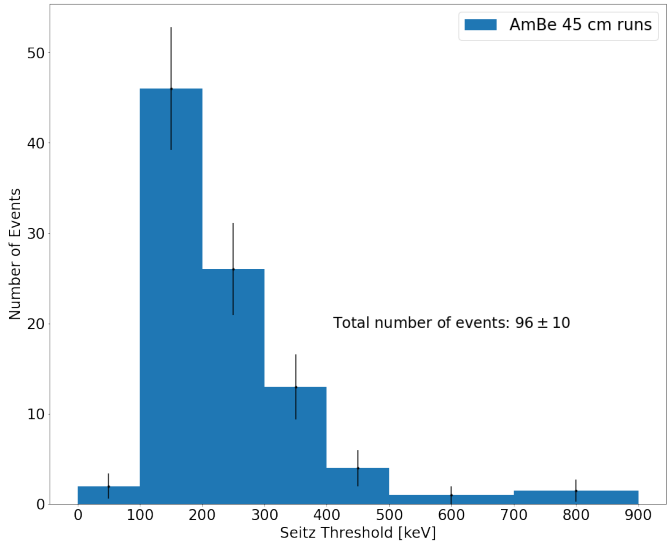

Figure 4.7: Event count vs Seitz thresholds at which the detector was operated for all the events reconstructed as bubbles in the AmBe dataset. Poissonian errors are assumed.

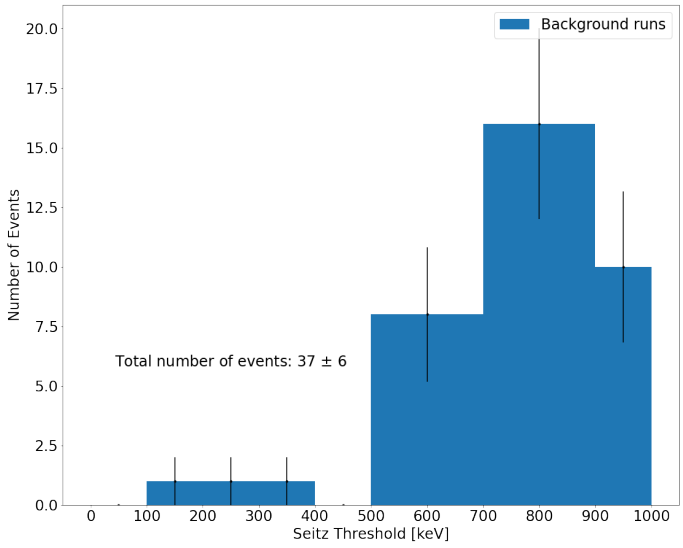

Figure 4.8: Event count vs Seitz thresholds at which the detector was operated for all the events reconstructed in the Background dataset. Poissonian errors are assumed.

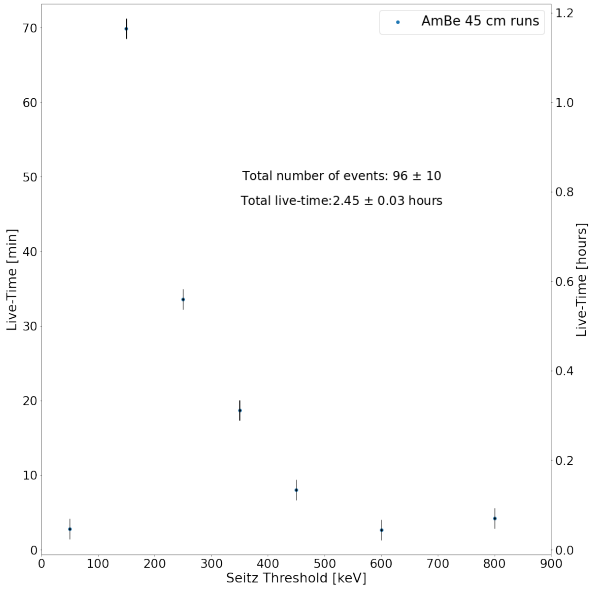

Figure 4.9: Live-time vs Seitz threshold for all events reconstructed as bubbles in the *AmBe* dataset.

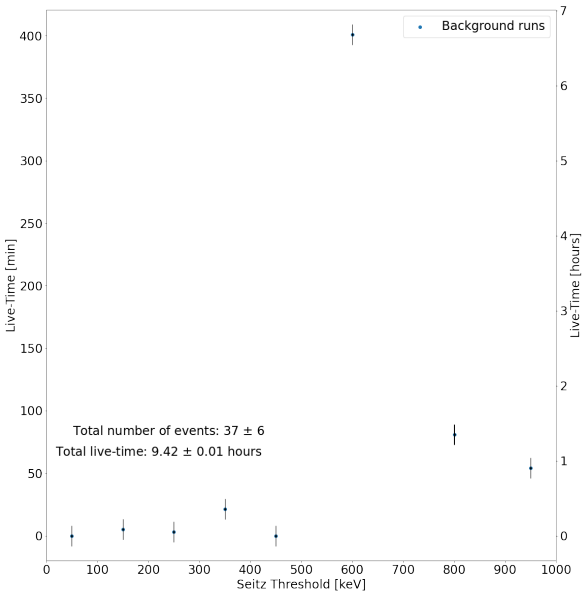

Figure 4.10: Live-time vs Seitz threshold for reconstructed events in the *Background* dataset.

The study of the event rate, by looking at the time differences between events, gives information on the dead time and efficiency of the detector. In figure 4.11, because periods between runs in the *AmBe 45 cm* runs did not register data, the time difference Δt between the end time and the start time of the runs is not taken into account. Instead, an exponential function, given by:

$$N = N_0 e^{-\Delta t \mu} \tag{4.4}$$

is fitted to the distribution of time differences between events because they are expected to be Poisson distributed [72]. In equation 4.4, N represents the number of events, N_0 a constant, and μ the mean event rate. In figure 4.11, fitting of equation 4.4 (green fit) gives a μ value of 11.0 ± 3.0 mHz (90.9 ± 27.3 s).

A second exponential distribution (black fit) with start at the second bin in figure 4.11 excludes the first with its dead time. The second μ value extracted from this fit is given by: 14.4 ± 3.8 mHz (69.4 ± 18.1 s). Likewise a third exponential distribution (purple fit) with start at the third bin in the same figure, gives a μ value of 12.3 ± 1.36 mHz (81.1 ± 9.0 s).

In figure 4.12, the Geant4 simulation of the same AmBe data neutron configuration shows a true exponential behaviour when examining the time differences between consecutive events. From this graph an event rate constant of 27.7 ± 4.4 mHz (36.1 ± 6.0 s) is extracted.

An approximation of the dead time effect is indicated by the dark and light cyan regions in figure 4.11. The sum of these regions corresponds to the prediction of events lost by taking the difference of the number of events between the black exponential fit excluding the first bin (61 events) and the measurement (19 events). This calculation suggests that 42 ± 6 events are lost. By repeating the same procedure for the purple exponential in figure 4.11, the prediction of events lost gives 15 ± 4. This is indicated as the dark cyan region in figure 4.11.

Adding the lost events to the observed events allows extracting a corrected

counting rate (R) for the black and purple exponential fits where the effects of dead time are more visible. For the black fit, the value of R:

$$R = \frac{(96 \pm 10) + (42 \pm 6) \text{ events}}{2.45 \pm 0.03 \text{ hours}} = \frac{138 \pm 12 \text{ net events}}{2.45 \pm 0.03 \text{ hours}} = 56.3 \pm 4.9 \frac{\text{net events}}{\text{hours}} \tag{4.5}$$

Likewise for the purple exponential fit,

$$R = \frac{(96 \pm 10) + (15 \pm 4) \text{ events}}{2.45 \pm 0.03 \text{ hours}} = \frac{111 \pm 11 \text{ net events}}{2.45 \pm 0.03 \text{ hours}} = 45.3 \pm 4.5 \frac{\text{net events}}{\text{hours}} \tag{4.6}$$

An estimate of the Geyser dead time (τ) can be calculated using the following equation:

$$R = \frac{\text{events measured}}{\text{live-time} - (\text{events measured})(\tau)} \tag{4.7}$$

where R is the corrected counting rate. The measured events and live-time for the neutron data taking are 96 ± 10 events and 2.45 ± 0.03 hours, respectively (see table 4.1). Therefore from equation 4.7 and R from the black exponential fit (equation 4.5),

$$\tau = 27.9 \pm 3.0 \text{ seconds} \tag{4.8}$$

Similarly. after applying equation 4.7 to the purple exponential fit (equation 4.6),

$$\tau = 12.4 \pm 1.1 \text{ seconds} \tag{4.9}$$

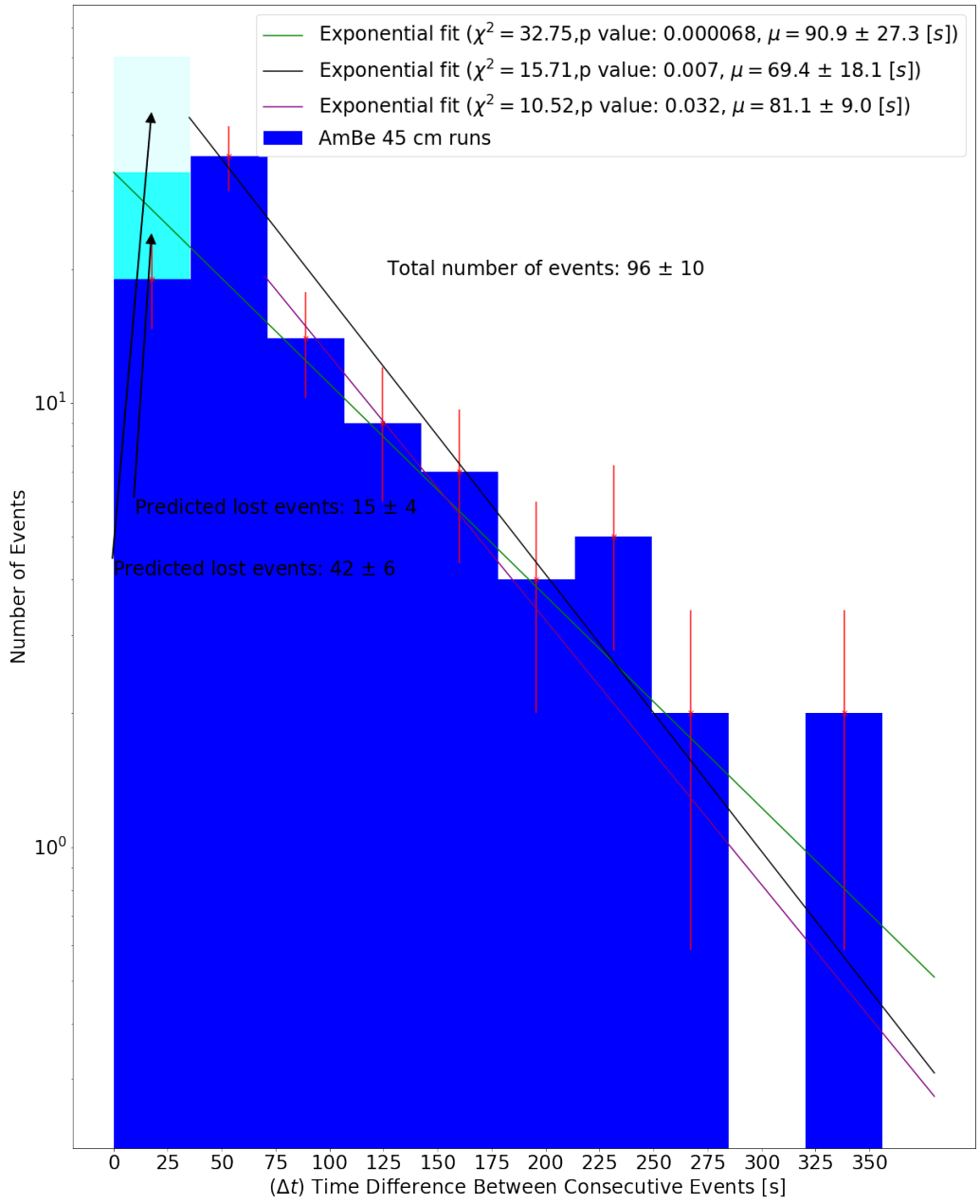

Figure 4.11: Time difference (Δt) between consecutive events in the *AmBe45 cm* runs dataset.

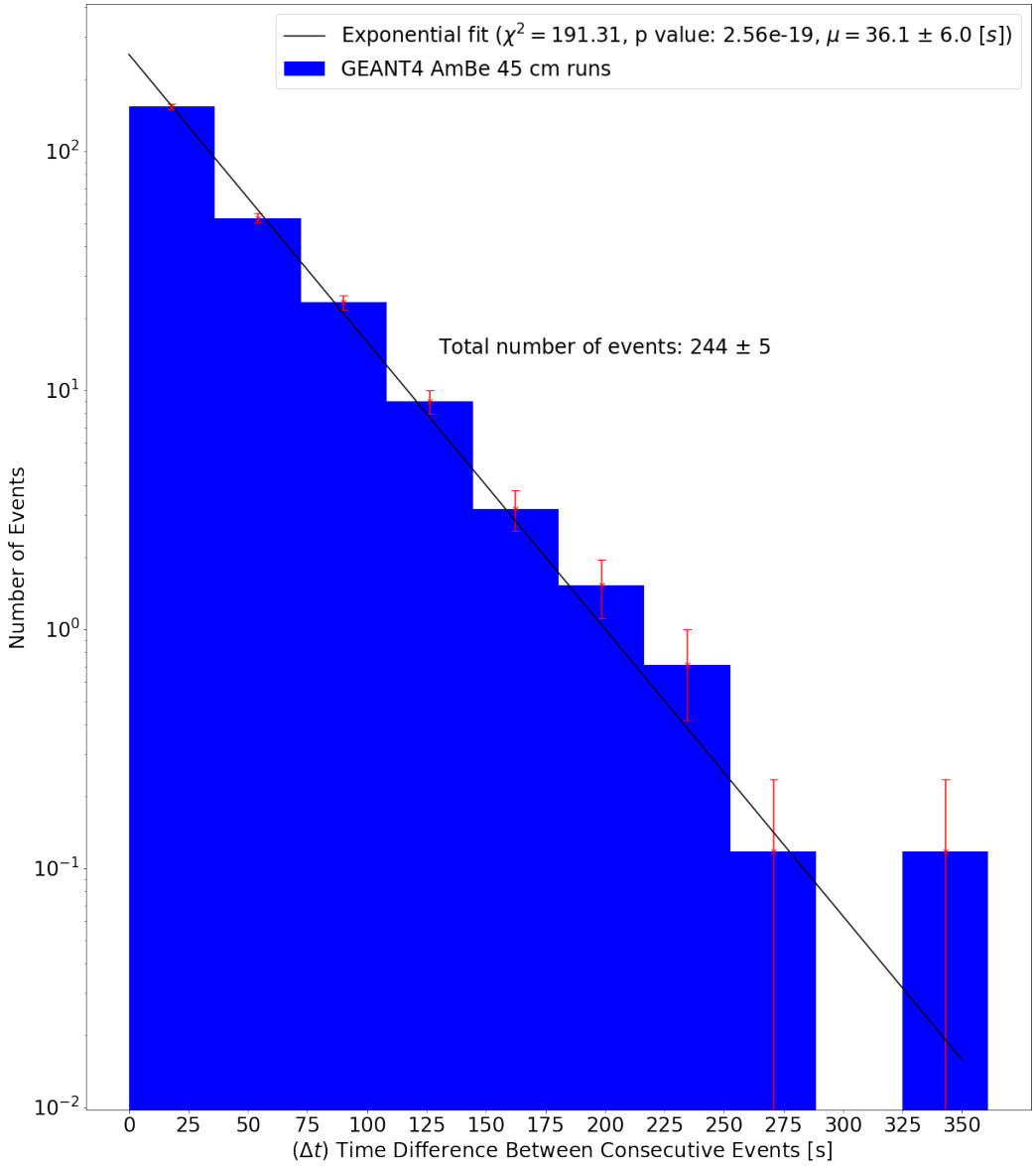

Figure 4.12: Time difference (Δt) between consecutive events in the Geant4 neutron simulations.

4.5 Detector response to Neutrons

The number of neutrons detected inside the Geyser active volume due to AmBe neutrons depends mainly on the neutron path inside the active medium, the geometry of the experiment (shape, size, distance between Geyser and AmBe source, etc) as well as precise knowledge of the neutron yield. All this knowledge can be encapsulated in the Seitz threshold (i.e thermodynamic parameters) as a function of the event rate.

Neutrons traversing a medium show an exponential attenuation [73]. Then, an exponential fit is used to study the Seitz threshold vs event rate (see figures 4.13, 4.14, and 4.15). The parameters of this model are,

$$\text{Event rate [mHz]} = Ae^{-\text{Seitz threshold [keV]}\lambda} \tag{4.10}$$

where,

- A: Event rate constant [mHz]
- λ: Threshold decay parameter $[keV^{-1}]$

These parameters provide an understanding of the response of the Geyser to AmBe neutrons. This is shown in figure 4.13, where the response of the detector decreases with increasing Seitz energy thresholds, as expected. In figure 4.14, the Geant4 Monte Carlo model of section 4.2 is used to validate the results from figure 4.13 (neutron data taking).

On the other hand, the event rate as a function of the Seitz threshold in the *Background* runs dataset is shown in figure 4.15. These events could be due to anomalous nucleation at the walls of the detector, fast neutrons from the environment, and natural radioactivity from detector materials. The main difficulty in explaining the background and a detailed study is that is sparse. In figure 4.15, to restrict the degrees of freedom in the fit of equation 4.7 to the *Background* runs, the threshold decay parameter of figure 4.14 is used as a fixed parameter.

4.6 Detector efficiency

Accurate absolute Geyser neutron measurements rely on the precise knowledge of their efficiency (ϵ) parameter. The value of ϵ is important for the extraction of numerical values of nuclear physics quantities (cross-sections, lifetime, branching ratio, etc).

The simplest method to determine ϵ is using a calibrated source of known strength [73]. This last statement is applicable to this experiment since the AmBe source used is well calibrated and studied (see reference [68] for details).

Mathematically ϵ is calculated as the solution of an integral over all possible final states of a nuclear process weighted with the probability to detect a given final state. Usually, the integrals cannot be solved analytically. Translated to Geyser terminology, the expected efficiency of the C_5F_{12} Geyser to neutrons ϵ, can be calculated as:

$$\epsilon = \frac{N_{obs}}{N_{sim}} \tag{4.11}$$

where:

- N_{obs}: The number of net events observed within the active volume (superheated C_5F_{12}) and that deposits energy above a certain energy threshold in a given unit of time.

- N_{sim}: The number of neutrons expected, based on the results of the simulation of the energy deposition within the active volume (superheated C_5F_{12}) above a certain threshold in a given unit of time.

The fact that neutron simulation and data taking have the same live-time (2.45 hours) and minimum Seitz threshold (72 keV), allows for a direct comparison of the events without further normalization.

The value of N_{obs} is calculated in 138 ± 12 events after dead time correction (equation 4.5). Likewise, $N_{sim} = 244 \pm 5$ events are extracted from the Geant4 simulation (figure 4.12). Putting those numbers into equation 4.11 gives a value of ϵ:

$$\epsilon = 56.5 \pm 5.0\ \% \tag{4.12}$$

An increase of the detector efficiency could be achieved by taking multiple scattering of neutrons into the calculations and neutron discrimination techniques (use of photography and sounds to ensure the nature of the bubble event).

To fully assess the detector efficiency, a careful study of the uncertainties of the thermodynamic parameters in the detector would be needed. This was not possible with the historic data used for this analysis.

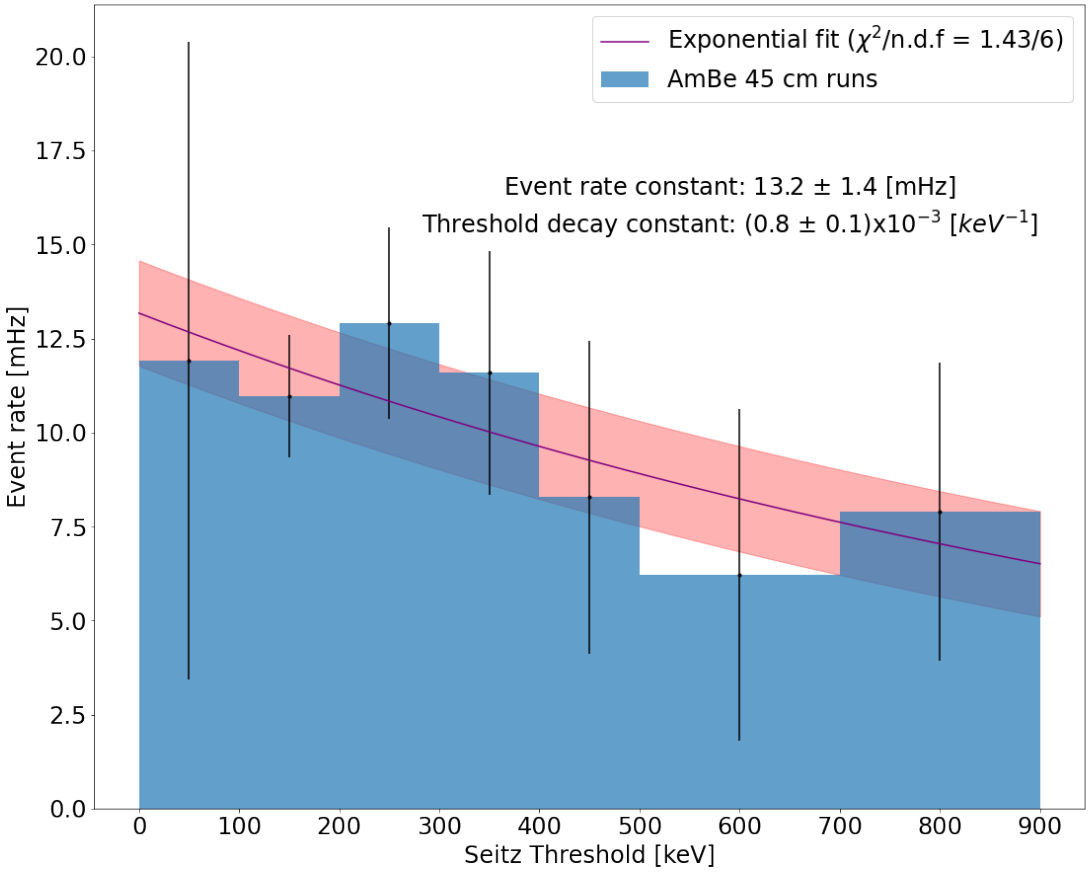

Figure 4.13: Event rate in the superheated C_5F_{12} when operated with the AmBe source. The red shaded area corresponds to ± 1 σ around the central fit values.

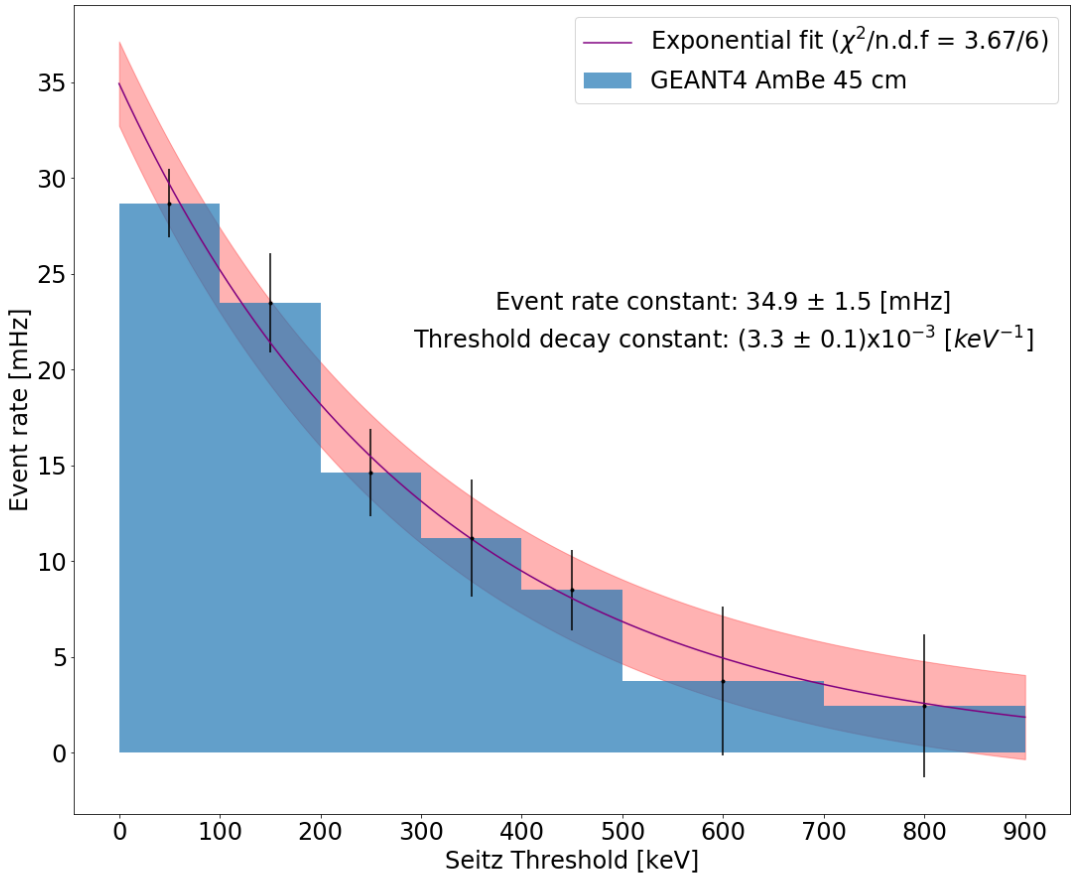

Figure 4.14: Seitz threshold vs Event rate in the Geant4 Simulation. The red shaded area corresponds to ± 1 σ around the central fit values.

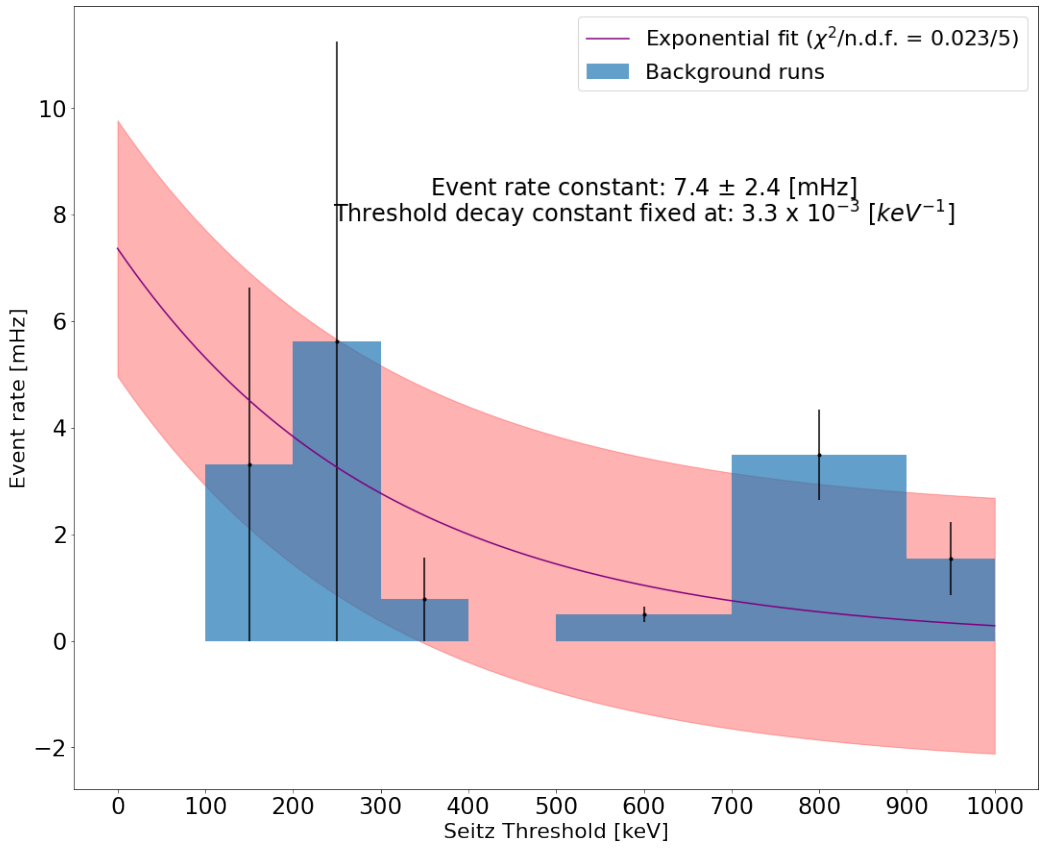

Figure 4.15: Event rate in the superheated C_5F_{12} caused by background nucleations. The red shaded area corresponds to ± 1 σ around the central fit values.

Chapter 5

Discussion and conclusions

5.1 Discussion

The low cost of a Geyser or compressionless bubble chamber filled with fluorocarbons, and the ease of commissioning and operation make them suitable workbenches for R&D for spin-dependent direct dark matter searches [74]. This superheated detector has the advantages of relative simplicity and low dead time. Additionally, the detector is practically free from manual operation and can have a fast recovery.

As with any other superheated technology, it is easy to scale to higher masses both in terms of complexity and cost. Even though, the superheated C_5F_{12} was not exposed to a gamma radiation field, the Geyser is expected to have a strong rejection of particles with minimum ionization (electrons and gamma recoils) as seen in other similar prototypes [75].

Possible items of future inquiry are presented in the next subsections.

5.1.1 High live-time in stable conditions

The detector stability in the 2018 data sets, demonstrated the functionality of the detector (see Chapter 3). All the data analyzed were taken without any improvements to the cooling of the top valve and the control of the liquid volume using the external hydraulic system (see figure 3.9, section 3.3.2, and section 3.3.3 for details). This extra cooling and volume control of the liquid was expected to have a large impact on the stability of the system (bubble growth size) at O(10) keV Seitz thresholds.

Unfortunately, this could not be explored due to COVID-19 related shutdowns of the laboratory activities at the University of Alberta.

5.1.2 Background identification and reduction

For achieving a good signal/background ratio, is important to characterize the backgrounds of all kinds.

There is a high chance that some of the events reconstructed during the neutron data taking, are not neutrons but instead bubble events associated with the fluid dynamics of the bubbles rising from the bottom to the top part of the bubble chamber. Its anecdotally reported that during data taking the manual pressure valve affected the amount of nucleation inside the C_5F_{12} Geyser. These two sources of bubbles are not taken into account in this study.

Regarding particle sources of nucleation, environmental neutrons represent the main source of background. For large exposures and stable operation of the detector, the environmental neutrons become a non-negligible source of background signals. As shown in Chapter 4, the Geant4 Monte Carlo implemented in this work, is a good representation of the neutron transport in the C_5F_{12} Geyser. Furthermore, this Monte Carlo could assist in modeling this background [1].

5.1.3 Hardware and software

Obtaining low Seitz energy thresholds rely on the thermodynamic properties of the gas pressure at the top of the Geyser. The volume control of the aforementioned region through a hydraulic system was constructed for this purpose and was part of the work of this thesis project. However, this idea was not tested.

In a future run of the Geyser, operation with the hydraulic system will enable bubble size control and enhanced stability. Is not only thought to be a tool to control the background due to anomalous nucleation but stabilize it in

[1] A tiny but not negligible source of fast and thermal neutrons are from cosmic rays. Simulations of this background are encouraged if exposures of the order of one year are achieved.

automatic mode.

The C_5F_{12} Geyser can also benefit from the camera and piezoelectric technology developed for the PICO bubble chambers. Those two additional channels of detection would add the possibility to inherently distinguish a neutron interaction from a recoil produced by alpha particles (mainly alphas from the Radon-222 chain).

5.2 Conclusion

As PICO-500 is being designed as the largest bubble chamber with the current technology, for multi-ton larger future chambers, a system that allows the operation of a bubble chamber without pressure control should be investigated.

The compressionless bubble chamber studied here has the potential of becoming a possible technology beyond PICO-500 chambers. For instance, a large number of compressionless bubble chambers operated together would have many of the advantages of a multiton bubble chamber.

In the meantime, this detector by itself can be explored further and improved as a novel approach to fast neutron detection in radiation dosimetry.

References

[1] The Planck Collaboration, "Planck 2015 results," *Astronomy and Astrophysics*, vol. 594, Oct. 2016. DOI: 10.1051/0004-6361/201525830.

[2] C. Patrignani *et al.*, "Review of Particle Physics," *Chin. Phys.*, vol. C40, no. 10, p. 100 001, 2016. DOI: 10.1088/1674-1137/40/10/100001.

[3] V. C. Rubin and J. Ford W. Kent, "Rotation of the Andromeda Nebula from a Spectroscopic Survey of Emission Regions,", vol. 159, p. 379, Feb. 1970. DOI: 10.1086/150317.

[4] F. Zwicky, "Republication of: The redshift of extragalactic nebulae," *General Relativity and Gravitation*, vol. 41, no. 1, pp. 207–224, 2009, ISSN: 00017701. DOI: 10.1007/s10714-008-0707-4.

[5] D. Perkins, *Particle Astrophysics, Second Edition (Oxford Master Series in Physics)*, 2nd ed., ser. Oxford Master Series in Physics. Oxford University Press, USA, 2009, ISBN: 0199545456.

[6] Clowe, Douglas; Bradač, Maruša; Gonzalez, Anthony H.; Markevitch, Maxim; Randall, Scott W.; Jones, Christine; Zaritsky, Dennis, "A direct empirical proof of the existence of dark matter," *The Astrophysical Journal*, vol. 648, 2 Sep. 2006. DOI: 10.1086/508162.

[7] M. Bradač, "Dark matter: Revealing the invisible with 2 cosmic supercolliders the bullet cluster 1e0657-56 and macsj0025-1222," *Nuclear Physics B - Proceedings Supplements*, vol. 194, pp. 17–21, none 2009, ISSN: 0920-5632. DOI: 10.1016/j.nuclphysbps.2009.07.002.

[8] M. Bradac, S. W. Allen, T. Treu, H. Ebeling, R. Massey, R. G. Morris, A. von der Linden, and D. Applegate, "Revealing the properties of dark matter in the merging cluster MACSJ0025.4-1222," *Astrophys. J.*, vol. 687, p. 959, 2008. DOI: 10.1086/591246. arXiv: 0806.2320 [astro-ph].

[9] V. Springel *et al.*, "Simulating the joint evolution of quasars, galaxies and their large-scale distribution," *Nature*, vol. 435, pp. 629–636, 2005. DOI: 10.1038/nature03597. arXiv: astro-ph/0504097.

[10] Kunz, Martin; Nesseris, Savvas; Sawicki, Ignacy, "Constraints on dark-matter properties from large-scale structure," *Physical Review D*, vol. 94, 2 Jul. 2016. DOI: 10.1103/PhysRevD.94.023510.

[11] Matthew Colless et al. the 2dFGRS team, "The 2dF Galaxy Redshift Survey: spectra and redshifts," *Monthly Notices of the Royal Astronomical Society*, vol. 328, 4 2001. DOI: 10.1046/j.1365-8711.2001.04902.x.

[12] Feng, Jonathan L., "Dark Matter Candidates from Particle Physics and Methods of Detection," *Annual Review of Astronomy and Astrophysics*, vol. 48, 1 Aug. 2010. DOI: 10.1146/annurev-astro-082708-101659.

[13] Peccei, R. D.; Quinn, Helen R., "Conservation in the presence of pseudoparticles," *Physical Review Letters*, vol. 38, 25 Jun. 1977. DOI: 10.1103/PhysRevLett.38.1440.

[14] A. Ringwald, "Exploring the role of axions and other WISPs in the dark universe," *Physics of the Dark Universe*, vol. 1, pp. 116–135, 1-2 2012, ISSN: 2212-6864. DOI: 10.1016/j.dark.2012.10.008.

[15] E. Zavattini et al., "PVLAS : probing vacuum with polarized light," *Nuclear Physics B - Proceedings Supplements*, vol. 164, pp. 264–269, none 2007, ISSN: 0920-5632. DOI: 10.1016/j.nuclphysbps.2006.11.096.

[16] Anastassopoulos, V. et al., "New CAST limit on the axion–photon interaction," *Nature Physics*, 2017, ISSN: 1745-2473,1745-2481. DOI: 10.1038/nphys4109.

[17] Braine, T. et al, "Extended search for the invisible axion with the axion dark matter experiment," *Physical Review Letters*, vol. 124, p. 101 303, 10 2020, ISSN: 0031-9007,1079-7114. DOI: 10.1103/PhysRevLett.124.101303.

[18] Rebecca K. Leane, "Dark matter theory and new searches," CAASTRO-CoEOO Workshop, 2017.

[19] K. Freese, "Status of dark matter in the universe," *International Journal of Modern Physics D*, Mar. 2017. DOI: 10.1142/S0218271817300129.

[20] L. Baudis, "Direct dark matter detection: The next decade," *Physics of the Dark Universe*, vol. 1, 1-2 Nov. 2012. DOI: 10.1016/j.dark.2012.10.006.

[21] J.D. Lewin; P.F. Smith, "Review of mathematics, numerical factors, and corrections for dark matter experiments based on elastic nuclear recoil," *Astroparticle Physics*, vol. 6, 1 1996. DOI: 10.1016/s0927-6505(96)00047-3.

[22] D. Tovey, R. Gaitskell, P. Gondolo, Y. Ramachers, and L. Roszkowski, "A new model-independent method for extracting spin-dependent cross section limits from dark matter searches," *Physics Letters B*, vol. 488, no. 1, pp. 17–26, Aug. 2000. DOI: 10.1016/s0370-2693(00)00846-7.

[23] D. G. Cerdeño, "Detection and identification of dark matter," *International Journal of Modern Physics Conference Series*, vol. 01, Jan. 2011. DOI: 10.1142/s2010194511000134.

[24] Klasen, M.; Pohl, M.; Sigl, G., "Indirect and direct search for dark matter," *Progress in Particle and Nuclear Physics*, Jul. 2015. DOI: 10.1016/j.ppnp.2015.07.001.

[25] F. Kahlhoefer, "Review of LHC dark matter searches," *International Journal of Modern Physics A*, vol. 32, 13 May 2017.

[26] M. W. Goodman, E. Witten, "Detectability of certain dark matter candidates," *Phys.Rev. D*, vol. 31, no. 3059, 1985. DOI: doi:10.1103.

[27] Gerard Jungman; Marc Kamionkowski; Kim Griest, "Supersymmetric dark matter," *Physics Reports*, vol. 267, pp. 195–373, 5-6 1996, ISSN: 0370-1573. DOI: 10.1016/0370-1573(95)00058-5.

[28] Undagoitia, Teresa Marrodán; Rauch, Ludwig, "Dark matter direct-detection experiments," *Journal of Physics G Nuclear and Particle Physics*, vol. 43, p. 013 001, 1 2016, ISSN: 0954-3899,1361-6471. DOI: 10.1088/0954-3899/43/1/013001.

[29] The PandaX Collaboration, "Dark Matter Results from 54-Ton-Day Exposure of PandaX-II Experiment," *Physical Review Letters*, vol. 119, p. 181 302, 18 2017, ISSN: 0031-9007,1079-7114. DOI: 10.1103/PhysRevLett.119.181302.

[30] The LZ Collaboration, "The LUX-ZEPLIN (LZ) experiment," *Nuclear Instruments and Methods in Physics Research Section A: Accelerators, Spectrometers, Detectors and Associated Equipment*, p. 163 047, 2019, ISSN: 0168-9002. DOI: 10.1016/j.nima.2019.163047.

[31] Akerib,D. et al., "Results of a Search for Sub-GeV Dark Matter Using 2013 LUX Data," *Physical Review Letters*, vol. 122, 13 Apr. 2019. DOI: 10.1103/PhysRevLett.122.131301.

[32] The XENON Collaboration, "The XENON1T dark matter experiment," *The European Physical Journal C*, vol. 77, p. 881, 12 2017, ISSN: 1434-6044,1434-6052. DOI: 10.1140/epjc/s10052-017-5326-3.

[33] The DEAP-3600 Collaboration, "Search for dark matter with a 231-day exposure of liquid argon using DEAP-3600 at SNOLAB," *Physical Review D*, vol. 100, p. 022 004, 2 2019, ISSN: 1550-7998,1089-4918. DOI: 10.1103/PhysRevD.100.022004.

[34] The DarkSide Collaboration, "Light yield in darkside-10: A prototype two-phase argon tpc for dark matter searches," *Astroparticle Physics*, vol. 49, pp. 44–51, 2013, ISSN: 0927-6505. DOI: 10.1016/j.astropartphys.2013.08.004.

[35] Aprile, E. and others, "Projected WIMP sensitivity of the XENONnT dark matter experiment," *JCAP*, vol. 11, p. 031, 2020. DOI: 10.1088/1475-7516/2020/11/031.

[36] Aalbers, J. et al, "DARWIN: towards the ultimate dark matter detector," *Journal of Cosmology and Astroparticle Physics*, vol. 2016, pp. 017–017, 11 2016, ISSN: 1475-7508,1475-7516. DOI: 10.1088/1475-7516/2016/11/017.

[37] The DarkSide Collaboration, "Low-mass dark matter search with the darkside-50 experiment," *Physical Review Letters*, vol. 121, p. 081 307, 8 2018, ISSN: 0031-9007,1079-7114. DOI: 10.1103/PhysRevLett.121.081307.

[38] R. Bernabei et al., "The DAMA/LIBRA apparatus," *Nuclear Instruments and Methods in Physics Research Section A: Accelerators, Spectrometers, Detectors and Associated Equipment*, vol. 592, pp. 297–315, 3 2008, ISSN: 0168-9002. DOI: 10.1016/j.nima.2008.04.082.

[39] The CDMS Collaboration, "Exclusion limits on the wimp-nucleon scattering cross-section from the cryogenic dark matter search," *Nuclear Instruments and Methods in Physics Research Section A: Accelerators, Spectrometers, Detectors and Associated Equipment*, vol. 444, pp. 345–349, 1-2 2000, ISSN: 0168-9002. DOI: 10.1016/s0168-9002(99)01388-1.

[40] The CRESST-III Collaboration, "First results on low-mass dark matter from the CRESST-III experiment," *Journal of Physics Conference Series*, vol. 1342, p. 012 076, 2020, ISSN: 1742-6588,1742-6596. DOI: 10.1088/1742-6596/1342/1/012076.

[41] The PICO Collaboration, "Data-driven modeling of electron recoil nucleation in PICO C3F8 bubble chambers," *Phys. Rev. D*, vol. 100, p. 082 006, 8 Oct. 2019. DOI: 10.1103/PhysRevD.100.082006.

[42] Felizardo, M. and Girard, T. A. and Morlat, T. and Fernandes, A. C. and Ramos, A. R. and Marques, J. G. and Kling, A. and Puibasset, J. and Auguste, M. and Boyer, D. and et al., "Final Analysis and Results of the Phase II SIMPLE Dark Matter Search," *Physical Review Letters*, vol. 108, no. 20, May 2012, ISSN: 1079-7114. DOI: 10.1103/physrevlett.108.201302.

[43] The PICASSO Collaboration, "Dark matter spin-dependent limits for WIMP interactions on 19F by PICASSO," *Physics Letters B*, vol. 682, 2 2009. DOI: 10.1016/j.physletb.2009.11.019.

[44] The PICO Collaboration, "Dark Matter Search Results from the PICO-2L C_3F_8 Bubble Chamber," *Physical Review Letters*, vol. 114, 23 Jun. 2015. DOI: 10.1103/PhysRevLett.114.231302.

[45] M. Ardid et al. PICO Collaboration, "Dark matter search results from the PICO-60 CF_3I bubble chamber," *Physical Review D*, vol. 93, no. 5, Mar. 2016, ISSN: 2470-0029. DOI: 10.1103/physrevd.93.052014.

[46] C. Amole et al. PICO Collaboration, "Dark matter search results from the complete exposure of the PICO-60 C_3F_8 bubble chamber," *Physical Review D*, vol. 100, no. 2, 2019, ISSN: 2470-0029. DOI: 10.1103/physrevd.100.022001.

[47] V. Kudryavtsev, "Background studies for dark matter experiments," *Nuclear Physics B - Proceedings Supplements*, vol. 173, none 2007. DOI: 10.1016/j.nuclphysbps.2007.08.042.

[48] D. Glaser, "Some effects of ionizing radiation on the formation of bubbles in liquids," *Physical Review (Series I)*, vol. 87, 4 1952. DOI: 10.1103/physrev.87.665.

[49] F. Becchetti, "History of the bubble chamber and related active- and internal-target nuclear tracking detectors," *Nuclear Instruments and Methods in Physics Research Section A: Accelerators, Spectrometers, Detectors and Associated Equipment*, vol. 784, pp. 518–523, 2015, ISSN: 0168-9002. DOI: 10.1016/j.nima.2015.01.030.

[50] B. Hahn, "The cavitation chamber," *Nuclear Physics B - Proceedings Supplements*, vol. 36, pp. 459–463, none 1994, ISSN: 0920-5632. DOI: 10.1016/0920-5632(94)90795-1.

[51] V. Zacek, "Search for dark matter with moderately superheated liquids," *Il Nuovo Cimento A (1971-1996)*, vol. 107, pp. 291–298, 2 1994, ISSN: 0369-3546,1826-9869. DOI: 10.1007/bf02781560.

[52] L. Bond; J.I. Collar; J. Ely; M. Flake; J. Hall; D. Jordan; D. Nakazawa; A. Raskin; A. Sonnenschein; K. O'Sullivan, "Development of bubble chambers with sensitivity to WIMPs," *Nuclear Physics B - Proceedings Supplements*, vol. 138, pp. 68–71, none 2005, ISSN: 0920-5632. DOI: 10.1016/j.nuclphysbps.2004.11.016.

[53] The COUPP4 Collaboration, "Bubble chamber operated in a deep underground site," *Physical Review D*, vol. 86, 5 Sep. 2012. DOI: 10.1103/PhysRevD.86.052001.

[54] The PICASSO Collaboration, "Discrimination of nuclear recoils from alpha particles with superheated liquids," 2008. DOI: 10.1088/1367-2630/10/10/103017.

[55] Bressler, M. and Campion, P. and Cushman, V.S. and Morrese, A. and Wagner, J.M. and Zerbo, S. and Neilson, R. and Crisler, M. and Dahl, C.E., "A buffer-free concept bubble chamber for PICO dark matter searches," *Journal of Instrumentation*, vol. 14, no. 08, P08019–P08019, Aug. 2019, ISSN: 1748-0221. DOI: 10.1088/1748-0221/14/08/p08019.

[56] Kozynets, Tetiana, Fallows, Scott and Krauss, Carsten B., "Sensitivity of the PICO-500 bubble chamber to supernova neutrinos through coherent nuclear elastic scattering," *Astroparticle Physics*, vol. 105, pp. 25–30, Feb. 2019, ISSN: 0927-6505. DOI: 10.1016/j.astropartphys.2018.09.004.

[57] M. Laurin, *Recherche de la matière sombre à l'aide de détecteurs à liquides surchauffés dans le cadre de l'expérience pico/picasso*, Montreal, Quebec, Mar. 2016.

[58] P. Mitra, *Development of a prototype for a low dead time dark matter detector using superheated liquid*, Edmonton, Alberta, Mar. 2013.

[59] A. Antonicci *et al.*, "MOSCAB: A geyser-concept bubble chamber to be used in a dark matter search," *Eur. Phys. J. C*, vol. 77, no. 11, p. 752, 2017. DOI: 10.1140/epjc/s10052-017-5313-8.

[60] F. Seitz, "On the theory of the bubble chamber," *Physics of Fluids*, vol. 1, 1 1958. DOI: 10.1063/1.1724333.

[61] B. Hahn and H. Reist, "The Geyser: A new detector for nuclear recoils (talk)," in *5th International Conference on High-Energy Physics and Nuclear Structure (ICOHEPANS)*, Jan. 1973, pp. 432–435.

[62] M. Volmer, *Kinetics of Phase Formation: (Kinetik Der Phasenbildung)*, ser. Chemische Reaktion. T. Steinkopff, 1939. [Online]. Available: https://books.google.ca/books?id=JWpoGwAACAAJ.

[63] S. C. Roy and B. Roy, "Use of superheated liquid in neutron detection," *Current Science*, vol. 84, no. 4, pp. 516–528, 2003, ISSN: 00113891.

[64] P. Reinke, *Surface boiling of superheated liquid*, Switzerland, Jan. 1997.

[65] *Chemical properties of n-perfluoropentane (cas 678-26-2)*. [Online]. Available: https://www.chemeo.com/cid/52-058-0/n-Perfluoropentane#ref-joback.

[66] S. Agostinelli et al., "GEANT4—a simulation toolkit," *Nuclear Instruments and Methods in Physics Research Section A: Accelerators, Spectrometers, Detectors and Associated Equipment*, vol. 506, pp. 250–303, 3 2003, ISSN: 0168-9002. DOI: 10.1016/s0168-9002(03)01368-8.

[67] K. Kluge H.; Weise, "The Neutron Energy Spectrum of a 241Am-Be (α, n) Source and Resulting Mean Fluence to Dose Equivalent Conversion Factors," *Radiation Protection Dosimetry*, vol. 2, pp. 85–93, 2 1982, ISSN: 0144-8420,1742-3406. DOI: 10.1093/oxfordjournals.rpd.a080571.

[68] Duke, M.J.M. and Hallin, A.L. and Krauss, C.B. and Mekarski, P. and Sibley, L., "A precise method to determine the activity of a weak neutron source using a germanium detector," *Applied Radiation and Isotopes*, vol. 116, pp. 51–56, Oct. 2016, ISSN: 0969-8043. DOI: 10.1016/j.apradiso.2016.06.032.

[69] John S. Hendricks; K.J. Adams; T.E. Booth; J.F. Briesmeister; L.L. Carter; L.J. Cox; J.A. Favorite; R.A. Forster; G.W. McKinney; R.E. Prael, "Present and future capabilities of MCNP," *Applied Radiation and Isotopes*, vol. 53, pp. 857–861, 4-5 2000, ISSN: 0969-8043. DOI: 10.1016/s0969-8043(00)00231-1.

[70] M.B. Chadwick, et al., "ENDF/B-VII.1 Nuclear Data for Science and Technology: Cross Sections, Covariances, Fission Product Yields and Decay Data," *Nuclear Data Sheets*, vol. 112, pp. 2887–2996, 12 2011, ISSN: 0090-3752,1095-9904. DOI: 10.1016/j.nds.2011.11.002.

[71] I. Antcheva et al, "ROOT — A C++ framework for petabyte data storage, statistical analysis and visualization," *Computer Physics Communications*, vol. 180, pp. 2499–2512, 12 2009, ISSN: 0010-4655. DOI: 10.1016/j.cpc.2009.08.005.

[72] W. Koehrsen, *The poisson distribution and poisson process explained*, Aug. 2019. [Online]. Available: https://towardsdatascience.com/the-poisson-distribution-and-poisson-process-explained-4e2cb17d459.

[73] Landsberger, Sheldon; Tsoulfanidis, Nicholas, *Measurement and Detection of Radiation, Fourth Edition*, 4th ed. CRC Press, 2015, ISBN: 978-1-4822-1548-9,1482215489.

[74] R. A. C. Anthony J. Peurring, "Bubble radiation detection: Current and future capability," Pacific Northwest National Laboratory, Richland, Washington, PNNL-13067, 1999.

[75] Bertoni, R. et al., "A new technique for direct investigation of dark matter," *Nuclear Instruments and Methods in Physics Research Section A: Accelerators, Spectrometers, Detectors and Associated Equipment*, vol. 744, Apr. 2014. DOI: 10.1016/j.nima.2014.01.026.